JGR Space Physics

Key Points:

- Magnetospheric substorm clusters produces energetic electron precipitation peaking in flux ~2 hr after onset
- The precipitation of >30 keV electrons has a well-defined pattern in Magnetic Local Time and L-shell, peaking in the morning sector
- Increasing AE geomagnetic disturbance is found to be a good proxy of both >30 and >300 keV peak precipitation flux for these events

Examination of Radiation Belt Dynamics During Substorm Clusters: Magnetic Local Time Variation and Intensity of Precipitating Fluxes

Craig J. Rodger[1] [ID], **Mark A. Clilverd[2]** [ID], **Aaron T. Hendry[1]** [ID], and **Colin Forsyth[3]** [ID]

[1]Department of Physics, University of Otago, Dunedin, New Zealand, [2]British Antarctic Survey (NERC), Cambridge, UK, [3]UCL Mullard Space Science Laboratory, Dorking, UK

Abstract Substorms are short-lived but significant reconfigurations of the geomagnetic field during which energetic particles are injected into the inner magnetosphere close to magnetic midnight. There is currently a need to quantify substorm-driven energetic electron precipitation (EEP) to better understand its role in radiation belt dynamics and to quantify its impact on the atmosphere. As substorm injections trigger chorus waves, which have strong MLT, AE, and L-shell dependence, we investigate the dependence of EEP in terms of these variables. We utilize many decades of low Earth orbit satellite observations to examine the typical statistical variability around substorm events identified by the Substorm Onsets and Phases from Indices of the Electrojet (SOPHIE) algorithm. In contrast to trapped flux enhancements, enhanced EEP is found to occur even for the quietest AE range of those considered (AE ≤ 100 nT, 100 nT < AE ≤ 300 nT, AE ≥ 300 nT). The MLT-dependent analysis for all AE-ranges shows a well-defined variation in >30 keV EEP magnitude, with a distinct and deep minimum in the late afternoon sector (15–18 MLT), and maxima in the mid to late morning sector (6–12 MLT). The patterns show similarities to previously published whistler-mode lower band chorus distributions with MLT. Clusters of substorms reliably produce enhancements in electron precipitation for >30 keV and >300 keV, with steadily increasing peak precipitation magnitudes with increasing AE. The peak precipitation flux L-shell also moves inwards with increasing AE, in a similar way for the two energy ranges.

1. Introduction

In the last decade, there has been significant and growing interest in the coupling of radiation belt electrons into the upper atmosphere through energetic electron precipitation (EEP). As well as being one of the competing processes driving the dynamic radiation belts, EEP has been linked to significant changes in the chemical composition of the stratosphere and mesosphere (e.g., Andersson et al., 2012, 2014; Gordon et al., 2020; Seppälä et al., 2007) potentially playing a role in regional climate variability (Baumgaertner et al., 2013; Seppälä & Clilverd, 2014; Seppälä et al., 2009). Because of these findings, recent efforts have been made to incorporate EEP into climate modeling codes (e.g., Van de Kamp et al., 2016; Matthes et al., 2017) and to better understand electron precipitation measurements from spacecraft and ground-based instruments (Asikainen & Ruopsa, 2016; Clilverd et al., 2010; Nesse Tyssøy et al., 2016; Nesse Tyssøy, Partamies, et al., 2021; Pettit et al., 2021; Rodger, Clilverd, et al., 2010; Rodger, Carson, et al., 2010; Rodger et al., 2012).

Electron fluxes in the outer radiation belt are highly dynamic, with much shorter lifetimes than in the inner belt (Claudepierre et al., 2020). The high dynamism in the outer belt is understood to be caused by competing drivers that lead to acceleration, loss, and transport. It is the combination of all of these competing processes that produce changes in the trapped fluxes. The occurrence and magnitude of the differing drivers are typically dependent upon the distribution of cold plasma density with distance from the Earth (often described through the L-shell parameter). This results in a clear delineation in the dynamics and losses of high-energy electrons at the plasmapause (e.g., Walton et al., 2021, 2022). However, these competing driving processes are also strongly dependent upon magnetic local time (MLT). The need to understand the spatial and temporal dynamism of the outer radiation belts encapsulates the primary science questions pertaining to that physical system (see, e.g., the recent review by Ripoll et al. (2020)).

Substorms are short-lived but significant reconfigurations of the geomagnetic field during which energetic particles are injected into the inner magnetosphere close to magnetic midnight (Akasofu, 1981; Cresswell-Moorcock et al., 2013). Approximately 50% of substorms result in an enhancement of the radiation belts (Forsyth et al., 2016)

and significant outer belt flux changes have been linked to clusters of substorms, termed "recurrent substorms". Outer belt electron fluxes following substorm clusters show much more significant flux increases than is observed in isolated substorm events (Rodger et al., 2016). Substorm injections lead to increases in whistler mode chorus wave activity, due to the enhancement of chorus "source" electrons with energies of 1–10s of keV (Baker et al., 1986; Jaynes et al., 2015; Reeves et al., 2013; Thorne et al., 2013). Recurrent substorm clusters have been shown to produce consistent enhancements in lower band whistler mode chorus (Rodger et al., 2016), the level of which is dependent upon geomagnetic activity seen through the AE index (Meredith et al., 2003, 2020; Rodger et al., 2022). Chorus is now recognized as a significant driver in outer belt electron acceleration (e.g., Jaynes et al., 2015; Simms et al., 2018). However, it has long been known that chorus elements are also efficient scatterers of radiation belt electrons, leading to precipitation spanning tens of keV up to several MeV (Hendry et al., 2012; Rodger, Clilverd, Thomson, et al., 2007; Thorne et al., 2010), dependent on MLT and L-shell due to the plasmasphere location and MLT-dependent varying chorus power (Whittaker et al., 2014).

The geomagnetic AE index is known to be a good indicator of the occurrence, strength, and duration of substorms (Borovsky, 2016; Gjerloev et al., 2004). As one might expect, clusters of substorms tend to occur during AE enhancements (Rodger et al., 2016), with stronger enhancements when the solar wind speeds are high (Rodger et al., 2022). Multiple studies have demonstrated that the pattern of intensity, occurrence, and MLT distribution of whistler mode chorus also varies with the AE index (e.g. Li et al., 2009; Meredith et al., 2003; Meredith et al., 2020). In addition, Nesse Tyssøy, Partamies, et al. (2021) reported that daily >42 keV electron precipitation is strongly correlated with the daily AE-index. Satellite observations of the occurrence of relativistic electron microbursts display MLT- and AE-dependent patterns consistent with those of whistler mode chorus (Douma et al., 2017), however the microburst magnitude do not show the same dependencies (Douma et al., 2019). In contrast, it has recently been reported that the spectral hardness of relativistic electron microbursts is AE-dependent, with more electrons at relatively higher energies when AE is enhanced (Johnson et al., 2021).

Thus there is increasing evidence that magnetospheric substorms, which are known to enhance chorus activity, lead to significant EEP into the atmosphere (Beharrell et al., 2015; Partamies et al., 2021). There is also evidence that multiple substorms should lead significant decreases in magnetospheric ozone (Seppälä et al., 2015), caused by substorm-triggered EEP spanning a wide range of magnetic latitudes (Cresswell-Moorcock et al., 2013). Ground based radar observations of ionospheric electrons and conductivity made before, during, and after substorm events show MLT-dependent responses (Stepanov et al., 2021). This latter study found that the response seen in the ionospheric D-region was stronger in the morning-dayside sector, which is consist with substorms triggering chorus in the morning MLT sector which in turn results in precipitation of electrons of 10s of keV.

In the current study we shift focus from trapped flux variations, as discussed in Rodger et al. (2022), to precipitating electrons linked to substorm clusters (as well as processes occurring before and after these clusters). As substorms trigger chorus waves which have strong MLT, AE, and L-shell dependence, we investigate the dependence of EEP in terms of MLT, AE, and L-shell. While it is very challenging to examine MLT processes occurring in-situ (Rodger et al., 2019), due to the rapid drift time of trapped radiation belt electrons "smearing out" event features, precipitating electrons are lost at a specific MLT, at least for strong scattering driving electrons into the bounce loss cone. As such it is possible to directly examine MLT-dependent processes through precipitating electrons measurements. As such it is possible to directly examine MLT-dependent processes through precipitating electrons measurements which are rapidly "smeared out" in trapped flux observations. We utilize many decades of low Earth orbit satellite observations to examine the typical statistical variability around these events. There is now a thrust in the radiation belt community to quantify precipitation loss to better understand its role in radiation belt dynamics. This is important to test physical theory, which should lead to improved radiation belt modeling, and also to better quantify the impact of EEP on the atmosphere and linkages to natural climate variability. The current work sits inside that wider community effort.

2. Experimental Datasets

2.1. POES SEM-2 Particle Observations

In the current study the electron precipitating flux data is provided by the Polar Orbiting Environmental Satellites (POES). These are a constellation of in ~100-min period Sun-synchronous polar Low Earth Orbits (LEO, ~800–850 km). The Space Environment Monitor (SEM-2) package (Evans & Greer, 2004) has been carried

onboard POES spacecraft from 1998 with the launch of NOAA-15. The NOAA POES spacecraft (i.e., NOAA-15, –16, −17, −18, and −19) all carry identical SEM-2 packages, as do the European MetOp-1 and -2 spacecraft. The European MetOp-3 spacecraft also includes the SEM-2, but data from this satellite only begins in 2019, and hence is outside the time period considered in the current study. The specific observations we use come from the Medium Energy Proton and Electron Detector (Evans & Greer, 2004; Rodger, Clilverd, et al., 2010; Rodger, Carson, et al., 2010), which provide both trapped and precipitating electron observations. For precipitating flux measurements at geomagnetic latitudes within (and polewards of) the radiation belts, we use the 0-degree telescopes (named 0eX, where X is the channel number (see Evans & Greer, 2004; Rodger, Clilverd, et al., 2010; for more details).

Our study focuses on the period from 1 Jan 2005 to 30 Nov 2018. Across that time window the number of SEM-2 carrying POES spacecraft launched mostly increased, although two satellites were lost during this period (NOAA-17 in 2013 and NOAA-16 in 2014). At the start of our time window there were three POES SEM-2 satellites (NOAA–15, –16, and –17), with five operational at the end of the time window (NOAA–15, –18, and –19, plus MetOp-1 and -2). The raw POES dataset has 2 s resolution, with simultaneous measurements from multiple spacecraft. In this time period there are 25,947 file days worth of POES SEM-2 satellite data, equivalent to ∼71 years of precipitating flux observations.

Due to the large number of POES spacecraft, and their LEO orbits, there is very good coverage across L and MLT (e.g., Hendry et al., 2016, Fig. 1). For the purposes of this study we have combined the MEPED observations from multiple POES satellites into a grid of median flux values binned by International Geomagnetic Reference Field (IGRF) L and time, taking 0.25 L-resolution and 15 min time resolution. This has also been undertaken for a series of MLT ranges: 0–3, 3–6, 6–9, through to 21–24 MLT. A more detailed description of the satellite dataset and the processing undertaken can be found in Rodger Clilverd, et al. (2010) and Cresswell-Moorcock et al. (2013).

2.2. SOPHIE Clusters of Substorms

In the current study we produce clusters of substorms where each substorm event is identified by the Substorm Onsets and Phases from Indices of the Electrojet (SOPHIE) algorithm (Forsyth et al., 2015). The SOPHIE algorithm examines the rate of decrease and increase of SuperMAG-L index (SML; Gjerloev, 2012; Newell & Gjerloev, 2011a) in order to identify substorm phases. The expansion phase of substorms are identified when the magnitude of the SML rate of decrease exceeds a given percentile threshold. We follow Rodger et al. (2022) and use the expansion phase onset times produced by the algorithm with a percentile threshold of 90. Clusters of substorms were produced using the same approach taken by Rodger et al. (2016, 2019), who themselves followed the definition and naming convention of Newell and Gjerloev (2011b). This leads to a set of onset times of substorm clusters or chains termed "recurrent" substorm groupings.

The substorm clusters used in the current study are identical to those used by Rodger et al. (2022) when they considered the dynamical changes of trapped electron fluxes seen in POES and GPS observations. The Rodger et al. (2022) report contains a more detailed explanation of the application of the SOPHIE algorithm, substorm selection, and clustering process, as well as the solar wind and geomagnetic index variations during the substorm clusters. For our time period of interest there were a total of 16,763 SOPHIE determined substorm expansion phases, leading to 2,749 recurrent substorm epoch start times, that is, 2,749 SOPHIE substorm clusters (2005–2018), an average of 197 per year.

3. Radiation Belt Trapped Electron Flux Dynamics

In an earlier study we examined how clusters of substorms were linked to dynamical variations of radiation belt trapped electron fluxes (Rodger et al. (2022)). We suggest that study should be viewed as a companion paper to the current report, as the earlier work made use of the sets of SOPHIE substorm clusters and AE-thresholds we employ here. As noted above it also contains details on the variation of solar wind and geomagnetic index variations during the substorm clusters. The primary difference between the earlier study and the current work is that the earlier study was entirely focused upon the dynamical changes of trapped radiation belt electrons, where-as the current study is entirely focused upon precipitating electrons and the AE- and MLT-dependent changes observed. The earlier study used POES LEO observations from the 90-degree telescopes; these are

dominated by trapped electrons in radiation belt geomagnetic latitudes (Rodger, Clilverd, et al., 2010; Rodger, Carson, et al., 2010). Contrasts were made with GPS-provided trapped flux electron observations from Medium Earth Orbit (MEO) to allow a major expansion in the energy range considered, spanning medium energy energetic electrons up to ultra-relativistic electrons. We direct the interested reader to the earlier companion paper, but provide a brief summary below due to the likely interaction between whistler mode chorus and electron precipitating losses causing dynamic changes in the trapped electron fluxes.

Rodger et al. (2022) undertook analysis of trapped radiation belt electron fluxes made at LEO and MEO before, during, and after substorm cluster start times. They found that clusters of substorms linked to moderate (100 nT < AE ≤ 300 nT) or strong (AE ≥ 300 nT) AE disturbances are associated with radiation belt flux enhancements. These clusters reliably occur during times of high speed solar winds streams with associated increased magnetospheric convection. The flux enhancements extended up to ultra-relativistic energies for the strongest substorms (as measured by strong southward B_z and high AE). However, substorm clusters associated with quiet AE disturbances (AE ≤ 100 nT) lead to no significant chorus whistler mode intensity enhancements, or increases in energetic, relativistic, or ultra-relativistic electron flux in the outer radiation belts. In these cases the solar wind speed was low, and the low geomagnetic Kp index indicated a lack of magnetospheric convection.

4. Radiation Belt Precipitating Electron Flux Dynamics

4.1. Overview

It is relatively common to examine various radiation belt processes (e.g., Aryan et al., 2020; Douma et al., 2019; Zhao et al., 2019) using the same three AE geomagnetic activity levels used in the chorus intensity studies (e.g., Meredith et al., 2003): quiet (AE ≤ 100 nT), moderate (100 nT < AE ≤ 300 nT), and strong (AE ≥ 300 nT). Given our focus on substorm clusters and EEP, it seems logical to apply the same AE activity levels. As noted above, information on the number of recurrent substorm clusters whose AE-values at onset correspond to the quiet to strong AE ranges can be found in Rodger et al. (2022, Table 1), along with detail on the variation with solar wind drivers, geomagnetic index changes, and trapped electron fluxes.

We undertake superposed epoch analysis (SEA) on POES-reported 0-degree telescope precipitating fluxes to determine the statistically "typical" behavior (i.e., median) of radiation belt losses into the atmosphere around recurrent substorm events. The SEA process should provide insight into the physical processes coupling the radiation belts and atmosphere. To do this, we take the zero epoch as the onset time of the first SOPHIE substorm expansion phase in each cluster, and examine the changes before, during, and after this event. We primarily focus on the >30 keV fluxes provided by the lowest energy channel in the POES MEPED suite of telescopes; these fluxes are expected to have the highest fluxes, and hence should be less hindered by the comparatively low sensitivity of these instruments (i.e., the noise floor at fluxes of 100 electrons cm^{-2} s^{-1} sr^{-1} (Rodger et al., 2013; Yando et al., 2011)).

Figure 1 shows an overview of the IGRF L-shell variation SEA for >30 keV precipitating fluxes in a ±1 day period around the cluster onset, separated by AE activity level. The left-hand side of Figure 1 shows the IGRF L-shell versus time plots, with the upper, middle, and lower rows corresponding to the quiet, moderate, and strong AE-ranges. Note that it is common in studies focused on the trapped radiation electron fluxes to narrow the range of L-shells considered to $L < 10$ (or less). However, substorm triggered EEP spans a much wider range of L-shells, requiring a much higher upper limit (Cresswell-Moorcock et al., 2013), hence, the chosen upper L-shell value of $L = 26$ for the left-hand panels in Figure 1. The right-hand side panels presents the median, quartiles, and confidence intervals for the left-hand side plots, restricted to an L-shell range of 5.0–15.0, for each of the corresponding AE-ranges. In the right hand side panels the superposed epoch median of the plotted parameter is given by the solid black line and the 95% confidence interval for this median is shown by the red band. The dark blue bands mark the interquartile range while the 95% confidence interval of this is shown in lighter blue.

The panels in Figure 1 shows well-defined differences as well as similarities in the variation of the precipitating radiation belt electron fluxes around the times of recurrent substorm clusters, depending on AE-level. In the case of the quietest AE-range (AE ≤ 100 nT, upper left panel), there is a clear decrease in the EEP flux starting just before the zero epoch, and reaching the smallest level at the zero epoch. This rapidly changes, however, to an increase in EEP flux spanning a wide range of L-shells, roughly $L \approx 5$–18, although the enhancement for L-shells above $L = 12$ only occurs for +1–4 hr after the zero epoch. The peak >30 keV EEP flux is at $L = 7.5$ and +2 hr
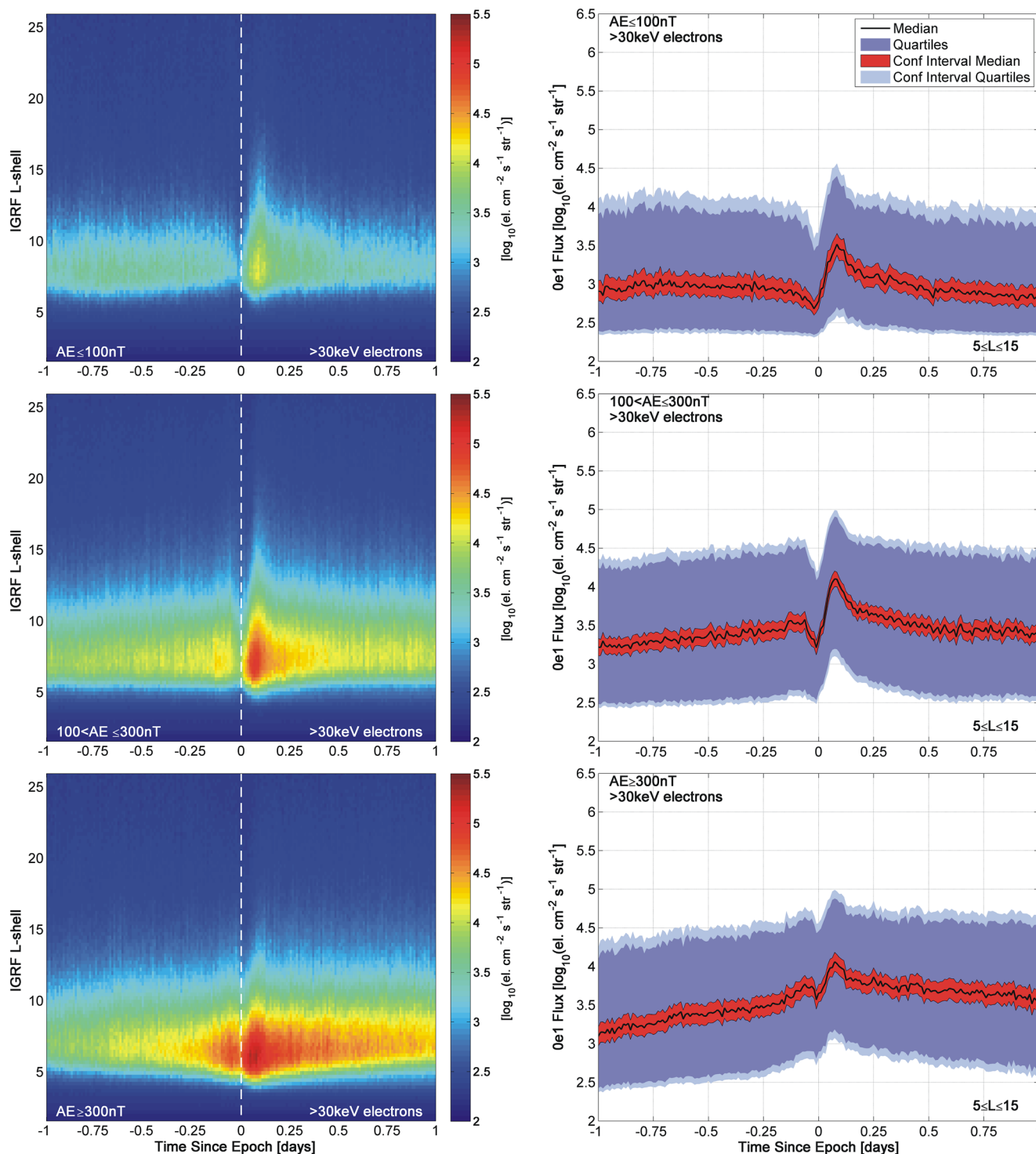
Figure 1. SEA showing the dynamics of the median >30 keV precipitating electron flux variation from POES. The SEA is considered separately for three geomagnetic activity levels, specified by AE index value at the time of zero epoch, which is the start of the substorm cluster. The left hand plots show the SEA of median precipitating electrons for the AE dependent recurrent Substorm Epochs, plotted against *L*-shell. The right hand plots show the statistical variation of the outer radiation belt >30 keV fluxes in the *L*-shell range from 5.0 to 15.0. In the right hand panels the superposed epoch median of the plotted parameter is given by the solid black line. The 95% confidence interval for this median is shown by the red band. The dark blue bands mark the interquartile range and the 95% confidence interval about it (light blue).

after the start of the substorm cluster (i.e., the zero epoch); the difference between the lowest and highest >30 keV flux magnitudes is slightly greater than one order of magnitude (i.e., 10 times). The left hand panel shows that the post-substorm cluster enhancement in EEP flux lasts until roughly +12 hr, at which point it has returned to "background" levels. The right panel is averaged over a wide L-shell range ($L = 5.0–15.0$), and shows the variation seen in the left-hand panels is consistent across the substorm epochs considered, with the brief EEP flux enhancement occurring in the median fluxes but also seen in the quartiles and the confidence intervals of those quartiles. Note that the confidence interval for the median is not large when compared with the magnitude of the EEP variation. While the changes are not particularly dramatic, they can be regarded as the statistically typical EEP response to clusters of substorms occurring during quiet AE conditions.

The middle panel of Figure 1 presents the SEA for the moderate AE conditions (100 nT < AE ≤ 300 nT). The left hand panel appears very similar to that shown for the quietest AE-range (AE ≤ 100 nT), except with larger magnitudes overall. For this AE range there is also a slow increase in >30 keV EEP in the 12 hr before the zero epoch (by about half an order of magnitude). Close to the zero epoch the EEP magnitudes start to drop, before rapidly increasing to a maximum level shortly thereafter. The maximum flux peaks at a larger magnitude than for quiet AE conditions, but also peaks very slightly earlier (at +1.5 hr). The peak moves inwards in L to 6.9 and in this case extends over a wider L-shell range (roughly $L \approx 4.5–20$) than when compared with the quiet AE conditions. The >30 keV precipitating flux remains slightly enhanced up to roughly +35 hr after the zero epoch, by which time the fluxes have returned to the same "undisturbed" conditions seen from −24 to −12 hr, before the zero epoch.

The moderate AE undisturbed precipitating flux magnitudes in the −24 to −12 hr time range are a few tenths of an order of magnitude higher than for the quiet cases, providing some evidence of "preconditioning". This is seen in the mid-right hand panel, with the initial median precipitating flux value ~0.2 higher in the mid-panel than the upper. The statistical response in the right hand panel also shows an increase in EEP magnitude during the run up to the zero epoch, which may be linked to the increasing solar wind speeds for these epochs (as reported by Rodger et al. (2022)). The statistical response averaged over $L = 5.0–15.0$ again shows a clear precipitation change around and following the zero epoch, with a decrease, sharp increase, and gradual recovery seen in the median, quartiles, and confidence intervals. The peak >30 keV precipitating flux magnitude averaged from $L = 5–15$ is ~0.6 of a flux magnitude order higher for quiet AE, both for the median values and the quartiles.

In contrast, the variation seen for epochs with strong AE (AE ≥ 300 nT) disturbances seen in the lower panel of Figure 1 show more enhanced flux magnitudes than for the moderate AE epochs, but with a less clearly well-defined variation than seen in the moderate (upper) and quiet (middle) AE condition panels. Aspects of the behavior are still similar to moderate AE, with a slow increase in flux magnitudes leading up to the zero epoch, a sharp decrease in EEP magnitude before the zero epoch, followed by a rapid increase in precipitation levels to higher levels and spanning a wider L-shell range, peaking shortly after the zero epoch. As in earlier panels, the L-shell of the peak EEP moves inwards with increasing AE, with the peak for the strong AE substorm clusters occurring at +1.25 hr and $L = 6.1$, that is, peaking earlier and moving inwards relative to the less active AE conditions in the upper panels. The peak EEP value is ~1.8 times (i.e., $10^{0.25}$) higher than the peak for moderate conditions, showing there is a strong increase in the substorm-linked EEP with increasing AE. However, in this case the peak does not have as well a defined pulse as seen for the quiet and moderate AE epochs. During the peak EEP pulse, which lasts from +0.25 to 3.5 hr, the EEP extends to even lower L-shells than seen in the less disturbed conditions, reaching $L \sim 3.5$. It is not clear, however, that the outer L-extent expands more, with enhanced fluxes only stretching out to $L \sim 19$ in the strong AE disturbances, whereas they extend out to $L \sim 22$ for the moderate AE range.

The statistical response averaged over $L = 5.0–15.0$ seen in the right hand panels are less well defined than the middle AE range. The averaging across the L-shells shows that the peak median and associated confidence intervals appear very similar to the moderate activity case. The principal difference between averaged moderate and high activity levels can be seen as a smaller zero epoch EEP decrease for the high activity case relative to the moderate case. Nonetheless the statistical response in this high AE activity case is essentially the same as the moderate AE range, if less well defined.

4.2. MLT Dependent Variations for All AE

It has long been recognized that radiation belt electron flux dynamics are impacted by multiple different processes which are themselves L and MLT-dependent. Examples are dayside magnetopause shadowing, substorms injecting energetic particles near magnetic midnight, and wave-particle interactions with plasma waves (occurring at differing MLT depending on the plasma wave MLT occurrence). Most of these processes are expected to act on timescales faster than the electron drift period. However, in-situ observations of these dynamical changes are challenged by the short drift times. Due to the large time length of the POES observational database, the satellites good MLT coverage, and the high number of substorm clusters considered here, we are in a position to examine the MLT dependence of precipitating electrons.

We now consider the MLT-dependent variation in >30 keV precipitating electrons, initially with no AE dependence. Figure 2 presents the results of the SEA undertaken for all the SOPHIE substorm clusters, separated into 3 hr MLT zones: 0–3, 3–6, 6–9, through to 21–24 MLT. The format of Figure 2 is essentially the same as the left hand panels of Figure 1, with the primary difference being the examination of the MLT-dependence of precipitating electron dynamics in Figure 2 rather than AE-dependence in Figure 1. Note that electron drift around the Earth is in the direction of increasing MLT.

It is immediately obvious that the MLT-dependence shown in Figure 2 is more dramatic than seen in the AE-dependence shown in Figure 1. The peak precipitating fluxes range from a deep low in the "late afternoon" 15–18 MLT sector (peak value 1.2×10^3 electrons cm^{-2} s^{-1} sr^{-1} at +3.5 hr after the zero epoch and $L = 6.1$) through to a strong maximum in the "early morning" 6–9 MLT sector (peak value 3.2×10^5 electrons cm^{-2} s^{-1} sr^{-1} at +1.7 hr after the zero epoch and $L = 6.9$). Note that while the peak precipitating flux occurs during the 6–9 MLT sector, the next MLT sector (9–12 MLT) is clearly more active in general, with only a slightly smaller peak flux value of 2×10^5 electrons cm^{-2} s^{-1} sr^{-1}. MLT dependence leads to a > 2 order of magnitude difference in peak precipitating >30 keV electron fluxes, along with significant variations in the L-shell range impacted.

There appears to be evidence of L-shell dependent dispersion with MLT. In the 0–3 MLT sector the precipitation enhancement appears to begin at the zero epoch time, ramping up rapidly to peak at +1 hr. Similar, if less strong variability is seen in the other "magnetic midnight" sector of 21–24 MLT. This variability likely reflects the start of the substorm cluster at the zero epoch, injecting electrons (potentially directly into the loss cone) and also triggering plasma waves leading to scattering and wave particle induced precipitation. In contrast, in the 9–12 MLT sector the enhancement onset starts at least 30 min later, peaking at +2 hr, with even longer delays occurring at higher and lower L-shells. The center of the enhanced precipitation in this sector is at about $L \sim 8$, for which a 30 keV electron with a 10° pitch angle (and thus near the loss cone edge), the drift period to complete a full Earth revolution is ~250 min. One would expect an electron to move through roughly a third of the total MLT range (i.e., from 0 to 3 to 9–12 MLT) in ~80 min, which is approximately consistent with the difference in the peak timing between the two sectors. However, the same electron would drift more quickly at $L = 10$ (drift period of ~180 min) and more slowly at $L = 6$ (drift period of ~300 min). This is not clearly seen in our SEA analysis, with the enhancement starting first in the $L \sim 8$ mid-L range and appearing later for both higher and lower L values. As such this behavior may be more dependent on the changing nature of the wave particle interactions than simple drift times.

The statistical variability of the >30 keV fluxes shown in Figure 2, and restricted to L-shells in the range of 5.0–15.0, are presented in Figure S1 in Supporting Information S1. The format of this figure is based on that of the right-hand side of Figure 1, showing the median, quartiles, and confidence intervals for the MLT range panels of Figure 2. These plots confirm the general MLT-dependent variability seen in Figure 2, with small enhancements in >30 keV EEP magnitudes following the zero epoch for the range 15–21 MLT (i.e., "late afternoon" to "mid evening"), and ~2 order of magnitude enhancements in precipitation for the range 6–12 MLT (i.e., "morning side"). While the quartiles and the 95% confidence intervals on the quartiles show large ranges before the zero epoch and from ~6 hr after the zero epoch, in the ~4–5 hr time period after the zero epoch there is a highly consistent increase in EEP across most MLT ranges. This suggests the variation seen in Figure 2 immediately following the start of a substorm cluster is highly reproducible, representing the typical changes in precipitation linked to these events. Note also that the 95% confidence interval around the median value has a small range immediately after the zero epoch, again indicating the high likelihood of such these enhancements.
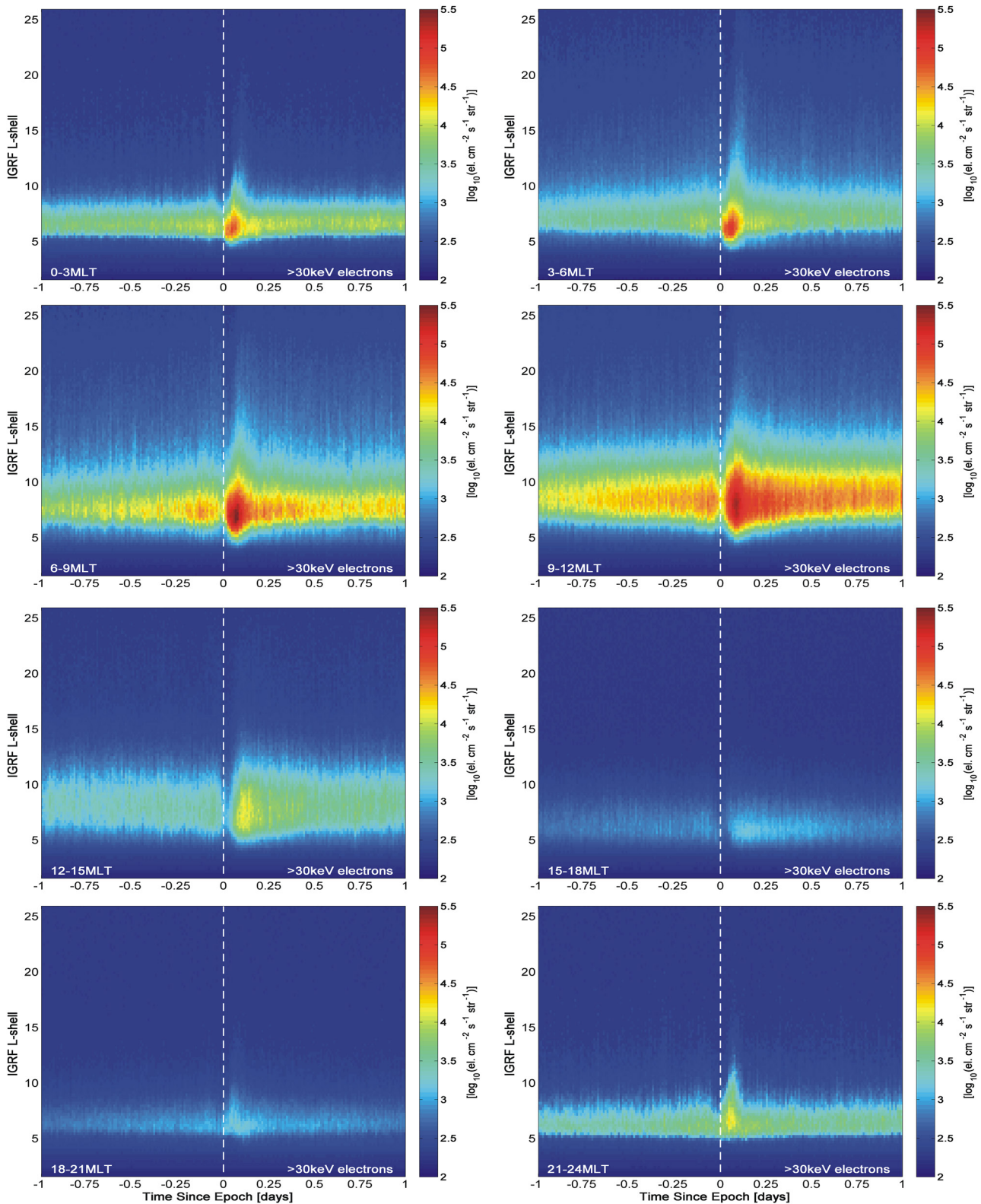
Figure 2. SEA showing the dynamics of the median >30 keV precipitating electron flux variation observed from POES, plotted against *L*-shell. The start of the substorm cluster defines the zero epoch, shown by the dashed white line in the panels. Each panel is for a different MLT range, as labeled. Note that electrons drift around the Earth from top-left to bottom-right. This SEA uses all the substorm clusters, without discriminating by AE.

4.3. AE- and MLT-Dependent Variations

As demonstrated in Figures 1 and 2, there are significant AE- and MLT-dependencies in the variation of >30 keV EEP magnitudes around substorm clusters, with particularly large variations across the MLT sectors. In an earlier study (Rodger et al., 2022), we showed that there were very significant differences in the dynamical variations in trapped flux around substorm clusters depending on AE ranges, and reported on the MLT dependence of trapped flux in Rodger et al. (2019). We now consider the AE- and MLT-dependencies in EEP for each of the three AE geomagnetic activity levels commonly used in chorus intensity studies (as described in Section 4.1).

#### 4.3.1. Quiet AE Disturbances (AE ≤ 100 nT)

Figure 3 presents the results of the SEA undertaken on the >30 keV EEP fluxes for the SOPHIE substorm clusters which have quiet AE levels at the zero epoch time. The format of Figure 3 is otherwise identical to Figure 2 (which included substorms with no AE discrimination). The variation in >30 keV EEP fluxes with MLT, IGRF L-shell, and epoch time are very similar between Figures 2 and 3, except that the flux magnitudes in Figure 3 are reliably smaller than the all-AE cases in Figure 2. It is notable that many of the finer details seen in the different MLT panels are the same when Figures 2 and 3 are contrasted, but with lower magnitudes. One example is the shape of the EEP enhancements shortly after the zero epoch. These are very similar when comparing the all-AE and quiet AE epochs, but with peak fluxes which are ~1.5–2 orders of magnitude lower in the case of the quiet AE epochs. The exception to this is in the MLT zones with the lowest flux magnitudes (i.e., 15–21 MLT), where the quiet AE precipitating fluxes are fairly close to the POES flux sensitivity threshold (~100 electrons cm^{-2} s^{-1} sr^{-1}) and the quiet AE peak fluxes are only ~0.5 orders of magnitude lower. Given the strong agreement between Figures 2 and 3, it is not surprising that the dominant MLT dependence and the >2 order of magnitude differences between morning-side and late afternoon/evening EEP levels are present in the low AE substorm clusters in much the same way as was seen for the all-AE case.

Given the expectation that whistler mode lower band chorus will be a significant driver of >30 keV EEP during and after substorms, it seems reasonable to contrast the MLT, L, and AE variation of EEP magnitudes shown in Figure 3 with those for equatorial whistler mode chorus intensity (e.g., Meredith et al., 2020, Figure 1). Note that we expect precipitation fluxes to scale linearly with the power of the plasma wave causing the pitch angle scattering (e.g., Rodger et al., 2003), as has been previously been confirmed in experimental observations (e.g., Rodger, Clilverd, Thomson, et al., 2007; Rodger, Clilverd, Seppälä, et al., 2010). For quiet AE conditions, Figure 1 of Meredith et al. (2020) indicates a ~2 order of magnitude difference in whistler mode lower band chorus intensity with varying MLT, with the lowest values in the MLT-range 18–21. In the morning and early afternoon MLT sectors there is enhanced chorus intensity extending to at least $L = 10$, which is the upper limit considered in the *Meredith* study. There is also a small enhancement seen in chorus intensities in the post-midnight MLT sector relative to pre-midnight, consistent with difference in EEP flux magnitude variation pre- and post midnight MLT. All of these lower band chorus characteristics are consistent with the MLT variations in EEP reported here.

The statistical variability of the quiet AE epoch >30 keV fluxes shown in Figure 3, restricted to L-shells range of 5.0–15.0, is presented in Figure S2 in Supporting Information S1.

4.3.2. Moderate AE Disturbances (100 nT < AE ≤ 300 nT)

Figure 4 presents the results of the SEA undertaken on the >30 keV EEP fluxes for the SOPHIE substorm clusters which have moderate AE levels at the zero epoch time. There are very strong similarities between Figure 4 and the all-AE case version of this plot (Figure 2), except that the moderate AE epochs show slightly stronger EEP magnitudes than seen in Figure 2. The moderate AE epochs EEP magnitudes are typically only 1–2 times larger than the all-AE case (i.e., essentially the same value or enhanced by up a factor of 2). A similar result was reported by Rodger et al. (2022) for the same epoch set when SEA was undertaken on trapped radiation belt fluxes; the variation for the moderate AE epochs was very similar to that for the all-AE case. Rodger et al. (2022) suggested this was because the all-AE SEA will be dominated by the events in the moderate AE range, as the moderate AE epoch set is the largest of the 3 groupings (Rodger et al., 2022, Table 1), making up ~47% of the total epochs. The MLT-dependent EEP variations seen in Figure 4 are similar with the changing lower band chorus wave reported for this AE range by Meredith et al. (2020, Figure 1). In particular, in that study the lowest chorus wave intensity are found shortly before 18 MLT (consistent with out 15–18 MLT panel). However, the highest EEP magnitudes are seen in the 9–12 MLT sector, while the equatorial lower band chorus intensity peaks in the ~2–6 MLT sector in Meredith et al. (2020; Figure 1), but from ~7 to 11 MLT in the earlier Meredith et al. (2012, Figure 4). As
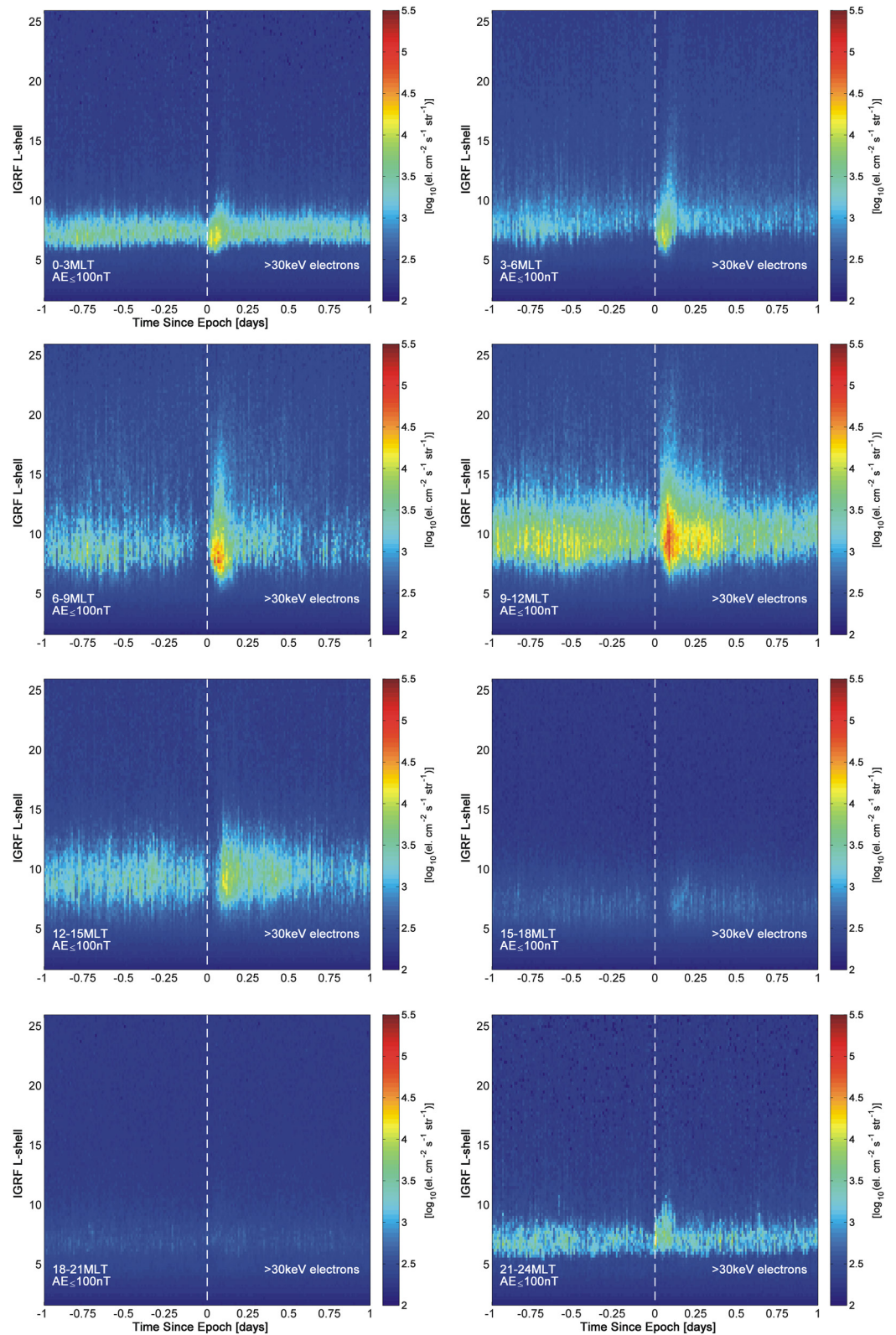
Figure 3. SEA of median >30 keV POES precipitating electrons for the Substorm Cluster Epochs, plotted against *L*-shell for zero epoch AE values in the range AE ≤ 100 nT (i.e., quiet). Each panel is for a different MLT range, as labeled. The format is otherwise as shown in Figure 2.
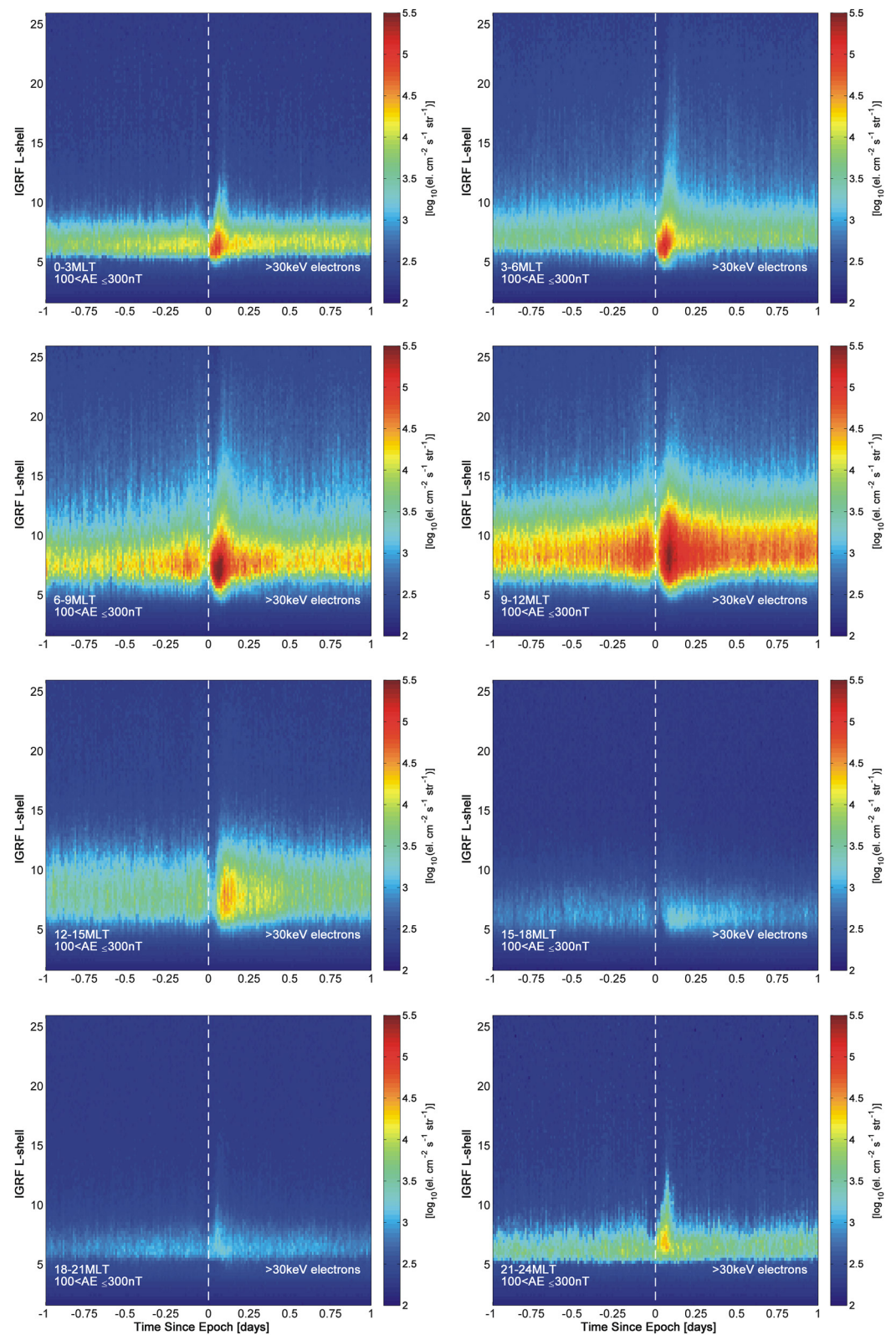
Figure 4. As Figure 3, but for the moderate AE range (100 nT < AE ≤ 300 nT).

such the EEP comparison with chorus observations presented in the most up to date literature is not dissimilar, but certainly not the same.

Figure 5 shows the statistical variation of the $L = 5$–15 fluxes plotted in Figure 4, following the same formatting used on the right hand side of Figure 1 as well as Figures S1 and S2 in Supporting Information S1. As expected, the differences between Figure 5 and the all-AE case (Figure S1 in Supporting Information S1) are rather small. Also as expected, the MLT-dependent pattern seen for quiet AE epochs (Figure 3 and Figure S2 in Supporting Information S1) are still present in Figure 5 in a consistent way, but with larger EEP magnitudes for the moderate AE range.

4.3.3. Strong AE Disturbances (AE ≥ 300 nT)

The SEA of >30 keV EEP magnitudes around the strong AE substorm cluster epochs is given in Figure 6. As expected from the lower left-hand panel of Figure 1, the MLT-dependent EEP magnitudes are larger than for the quiet and moderate ranges (Figures 3 and 4), and also larger than the all-AE case (Figure 2). The fundamental MLT-dependent pattern in the variation of EEP around the substorm cluster epochs is not significantly different, but as seen in the lower left-hand panel of Figure 1, it is less clearly defined than for the quiet and moderate AE level epochs. When the strong AE and all-AE SEA results are contrasted there is an increase in the strong EEP magnitudes at most MLT by ∼1.5-2 orders of magnitude for radiation belt L-shells (i.e., L ∼ 4–7), and also for time periods outside of the main substorm cluster activity (i.e., 0–0.2 days equivalent to 0–5 hr). Inside the time period dominated by the substorm cluster the EEP levels are much more similar, as expected from the comparisons shown in Figure 1. The significant differences between the strong AE and all-AE SEA results before the zero epoch is likely due to preconditioning, as discussed below.

When contrasted with Figure 3 or 4, there is evidence in Figure 6 of preconditioning in the EEP magnitudes before the zero epoch at essentially all MLT sectors, that is, slowly growing EEP magnitudes in the 12–24 hr before the cluster onset, followed by a sharp change associated with the substorm cluster. This was noted earlier in our study focused on trapped flux changes at LEO and MEO around the occurrence of the same substorm cluster epoch list (Rodger et al., 2022); in that study it was suggested the preconditioning might be linked increasing pre-zero epoch convection, as evidenced by the SuperMAG AU and Kp values before the zero epoch time (Rodger et al., 2022, Figure 3). Such convection would be expected to stimulate additional chorus wave activity before the substorm, which would lead to enhanced >30 keV EEP and drive changes in trapped radiation belt fluxes. We suggest this would be a worthy subject for a future study, making use of in-situ plasma wave datasets.

The MLT-dependent pattern of changing EEP in Figure 6 is very similar to that seen earlier (i.e., in Figures 2–4), other than what appears to be steadily increasing EEP magnitudes with increasing AE, and possible preconditioning. When contrasted with the MLT and L-dependence of lower band whistler mode chorus intensities (Meredith et al., 2012, Figure 4; Meredith et al., 2020, Figure 1), there is broad agreement, with orders of magnitude more activity in the late morning to early afternoon sectors when compared with late afternoon to early afternoon sectors. However, there is not a detailed one to one correspondence between the AE-dependent lower band whistler mode chorus intensities from the literature and the >30 keV EEP magnitudes presented in the current study.

Figure 7 shows the statistical variation of the $L = 5$–15 EEP fluxes plotted in Figure 6, following the same formatting used in Figure 5 and similar previous figures. When averaged over this wide L-shell range the peak EEP fluxes are similar to those seen in Figure 5, and in some cases slightly smaller. The variability is not as clear as previously seen for quiet epochs (Figure S2 in Supporting Information S1) or moderate (Figure 5), suggesting that the EEP produced by the high-AE substorm cluster is not as clearly dominant when contrasted with other processes occurring before, during, and after the cluster. That may be caused by pre-cluster convection driving by high speed solar winds which typically occur around this set of epochs (Rodger et al., 2022, Figure 3). It seems important to note that the patterns seen previously are not absent, as was clear from Figure 6, only that these EEP variability patterns are not as clearly defined.

4.3.4. Overview

From the SEA conducted in the sections above, we conclude that the MLT dependence is not particularly AE sensitive. There is, however, a clear AE dependence in terms of the peak EEP magnitudes (i.e., higher AE linked to larger EEP peaks) and weak levels of preconditioning (i.e., higher AE levels show higher EEP before, as well
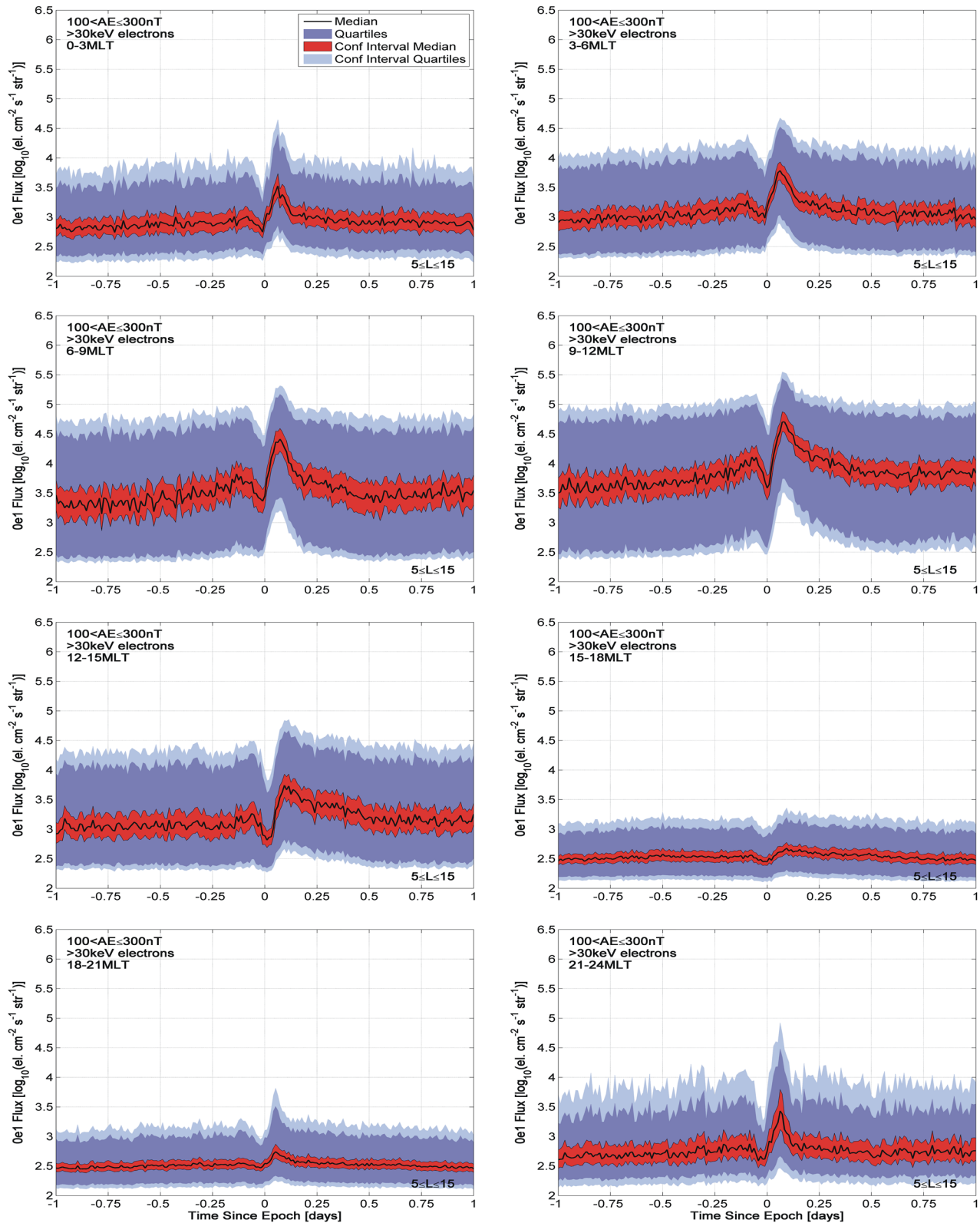
Figure 5. Statistical variation of the >30 keV precipitating fluxes in the *L*-shell range from 5.0 to 15.0 for the flux variations shown in Figure 4 (i.e., zero epoch AE values in the range 100 nT < AE ≤ 300 nT). The median, quartiles, and confidence intervals are plotted in the same format as the right hand panels of Figure 1.

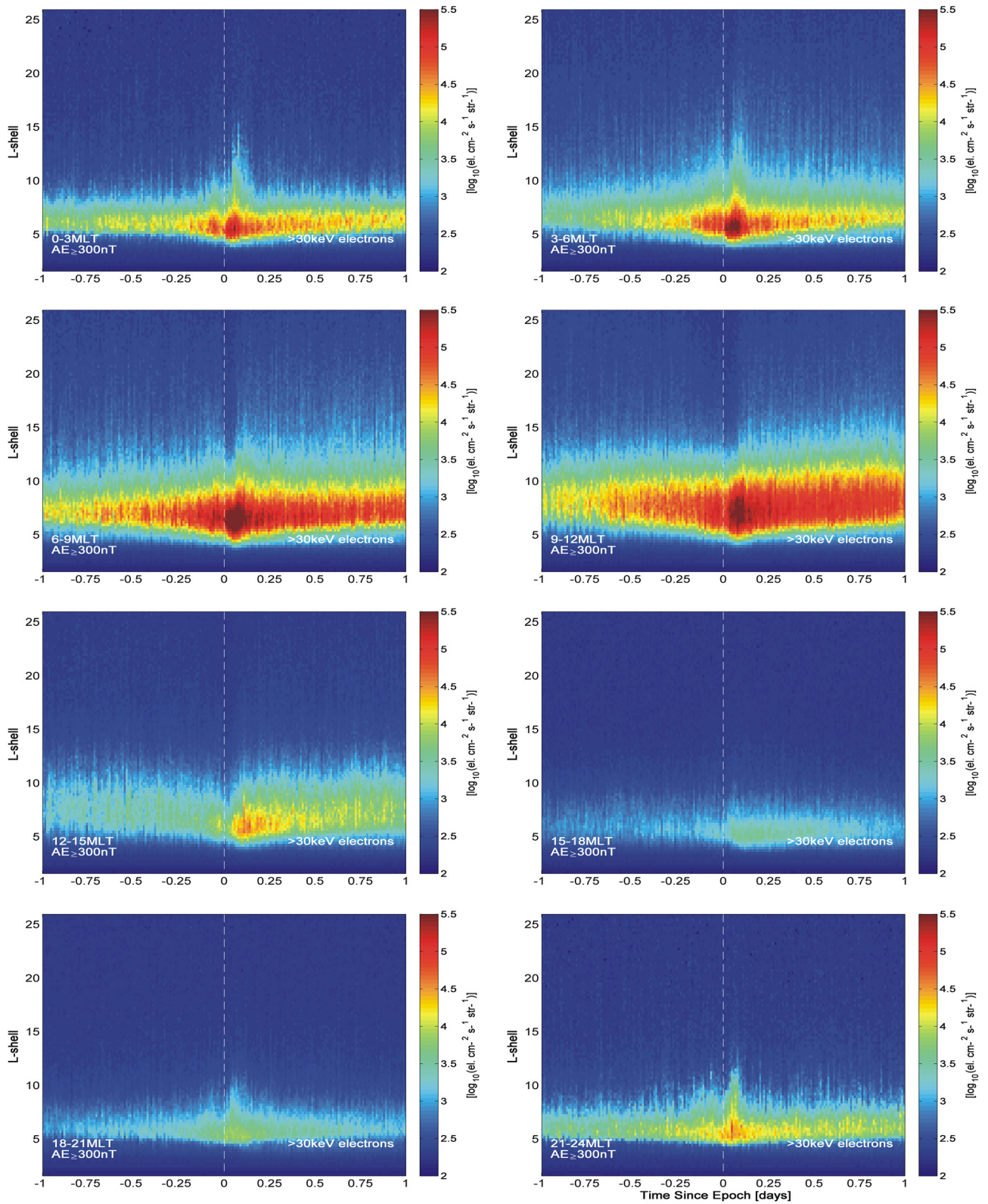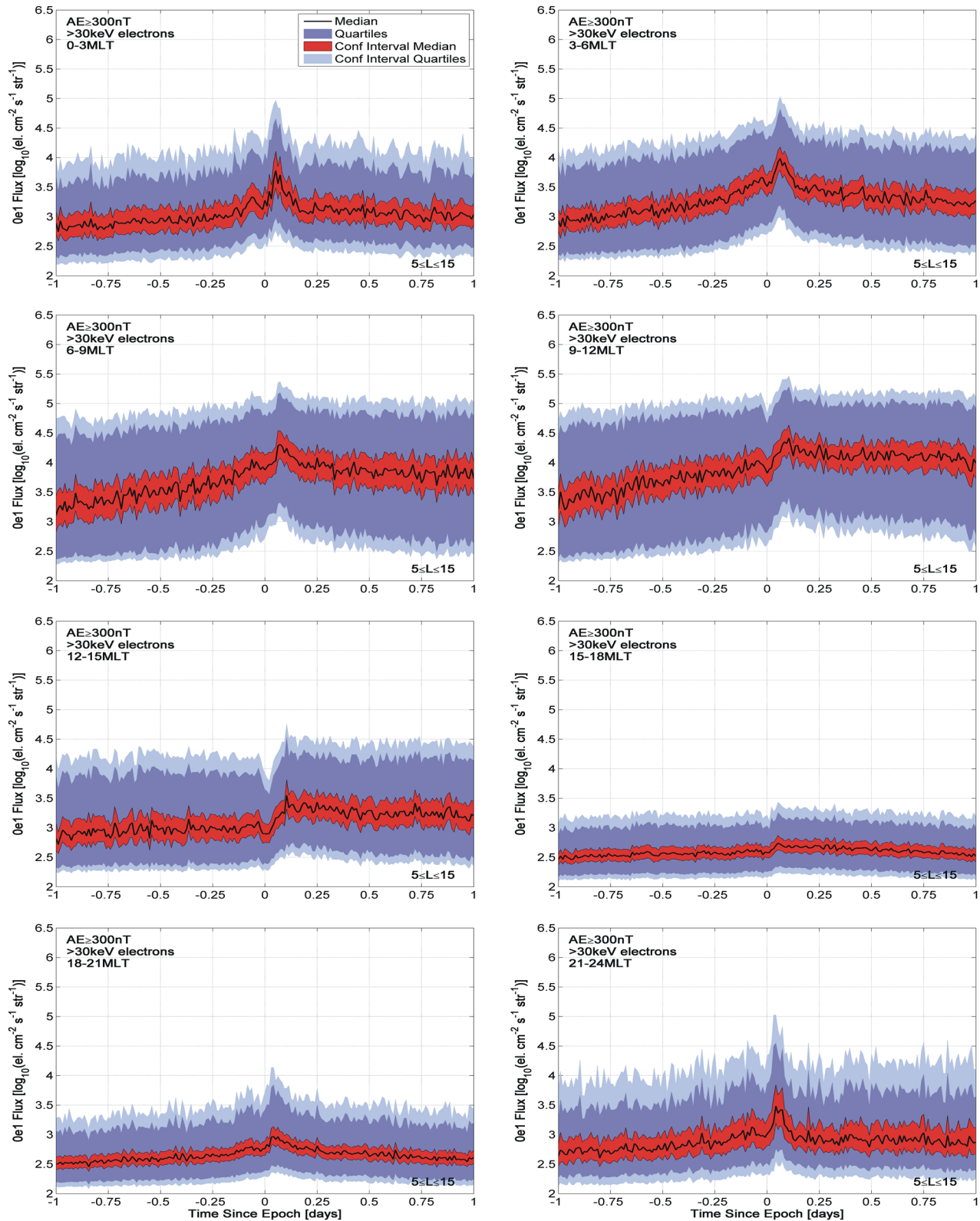**Figure 6.** As Figures 3 and 4, but for the strong AE geomagnetic disturbance range (AE ≥ 300 nT).

Figure 7. Statistical variation of the >30 keV precipitating fluxes in the *L*-shell range from 5.0 to 15.0 for the flux variations shown in Figure 6 (i.e., zero epoch AE values in the range ≥300 n). This figure is in the same format as Figure 5 and the right hand panels of Figure 1.

as after, the zero epoch substorm cluster start time). In Section 5 we examine the AE dependence on the peak flux magnitudes in greater detail.

5. Variation of EEP With Increasing AE Activity

The analysis presented in Section 4 indicates that the magnitude of the >30 keV EEP flux depends on whether the substorm cluster is linked to AE-levels which are quiet, moderate, or strong. Recently, Nesse Tyssøy, Partamies, et al. (2021) reported that daily averaged >30 keV fluxes were strongly correlated with daily AE geomagnetic values, but that the higher energy MEDPED observations from the 0e3 channel (nominally >300 keV electrons) were poorly predicted by changing AE. Given the clear AE-dependent patterns seen in Figures 1–6, we investigate the detailed AE-dependence of the 0e1 (>30 keV) and 0e3 (>300 keV) observations below. The comparatively large number of substorm clusters in the SOPHIE produced epoch list means it is practical to make a more detailed investigation of the AE dependence (neglecting MLT variation), moving away from the broad AE groupings commonly used to consider whistler mode chorus and other radiation belt processes.

5.1. >30 keV Medium Energy Electron Precipitation

Figure 8 presents our investigation into changing EEP magnitudes following the start of substorm clusters, and the variation with the AE value taken at the start of the cluster, that is, the zero epoch. This is essentially the same as the broad AE groupings considered in Section 4, but we now sweep through AE using a much smaller AE step-size, in this case only 25 nT. There are sufficient substorms and observations to allow meaningful analysis from 0 to 750 nT.

The top left panel of Figure 8 provides an example of the changing EEP magnitudes for one of the smaller AE steps, in this case the SEA of the >30 keV EEP for the AE range from 200 to 225 nT. Only the time period from −1 to +5 hr is shown, otherwise the format is the same as the left-hand panels in Figure 1. This SEA results for 200–225 nT shown in this panel is very similar to the same time period of the moderate AE range (100 nT < AE ≤ 300 nT) seen in the middle left-hand panel of Figure 1. The primary differences are that in Figure 8 the variability is less smooth than for the panel in Figure 1, due to the smaller AE range and lower number of substorm clusters included (1,283 moderate clusters cf. 213 clusters in the range 200–225 nT). For each 25 nT AE range, we sum the flux across all L-shells (this analysis was undertaken from 1.5 to 30), and determine the epoch time where this is maximum. For the L-varying EEP at the epoch time of maximum summed EEP, we find the peak flux value, and the L-shell at which this occurs, along with the statistical variation in the peak flux values (i.e., confidence intervals and quartiles). As an example, for the AE range shown in the upper left hand panel of Figure 8 with mid-point AE = 212.5 nT, the maximum summed EEP flux time was +1.75 hr after the zero epoch, with the maximum >30 keV EEP flux at this epoch time occurring at $L = 7.1$, with a value of 1.5×10^5 electrons cm^{-2} s^{-1} sr^{-1}.

The lower left panel of Figure 8 shows the L-varying EEP at the epoch time of maximum summed EEP for each 25 nT AE bin in our range. At the lowest AE levels EEP magnitudes are small, but clearly above the MEPED noise floor. This panel suggests the EEP magnitudes rise steadily with increasing AE indicating that the AE at the start of a substorm cluster is a good proxy for the EEP fluxes occurring during the cluster. This may be useful for future investigations into the importance of substorms on atmospheric chemistry, dynamics, and climate coupling (i.e., building on previous work, examples being Seppälä et al. (2007, 2009, 2015) and Matthes et al. (2017)). This panel shows that for >30 keV fluxes, the substorm linked precipitation extends well beyond the traditional range of the radiation belts, out to beyond $L = 15$ (particularly for mid-AE range substorms). It is also clear that the L-shell of the peak EEP flux moves inwards with increasing AE, from $L \sim 8$ at lowest AE levels in to L of 5–6 at the highest AE; this is plotted in the left-hand panel of Figure S3 in Supporting Information S1. We note that the inward motion of the peak EEP location and the AE dependence is consistent with Figure 1, but is considerably clearer due to the smaller AE-ranges.

In the lower right-hand panel of Figure 8 we examine in more detail the AE dependence and statistical variability of the peak >30 keV EEP flux magnitudes linked to substorm clusters. This figure shows the maximum flux value for the time and L-shell of the peak. The colors used are the same as those employed in previous statistical plots, for example, the right hand panels of Figure 1. As noted for the lower left-hand panel of Figure 8, the peak >30 keV EEP fluxes increase with AE, in an essentially monotonic fashion. Across the AE range considered,
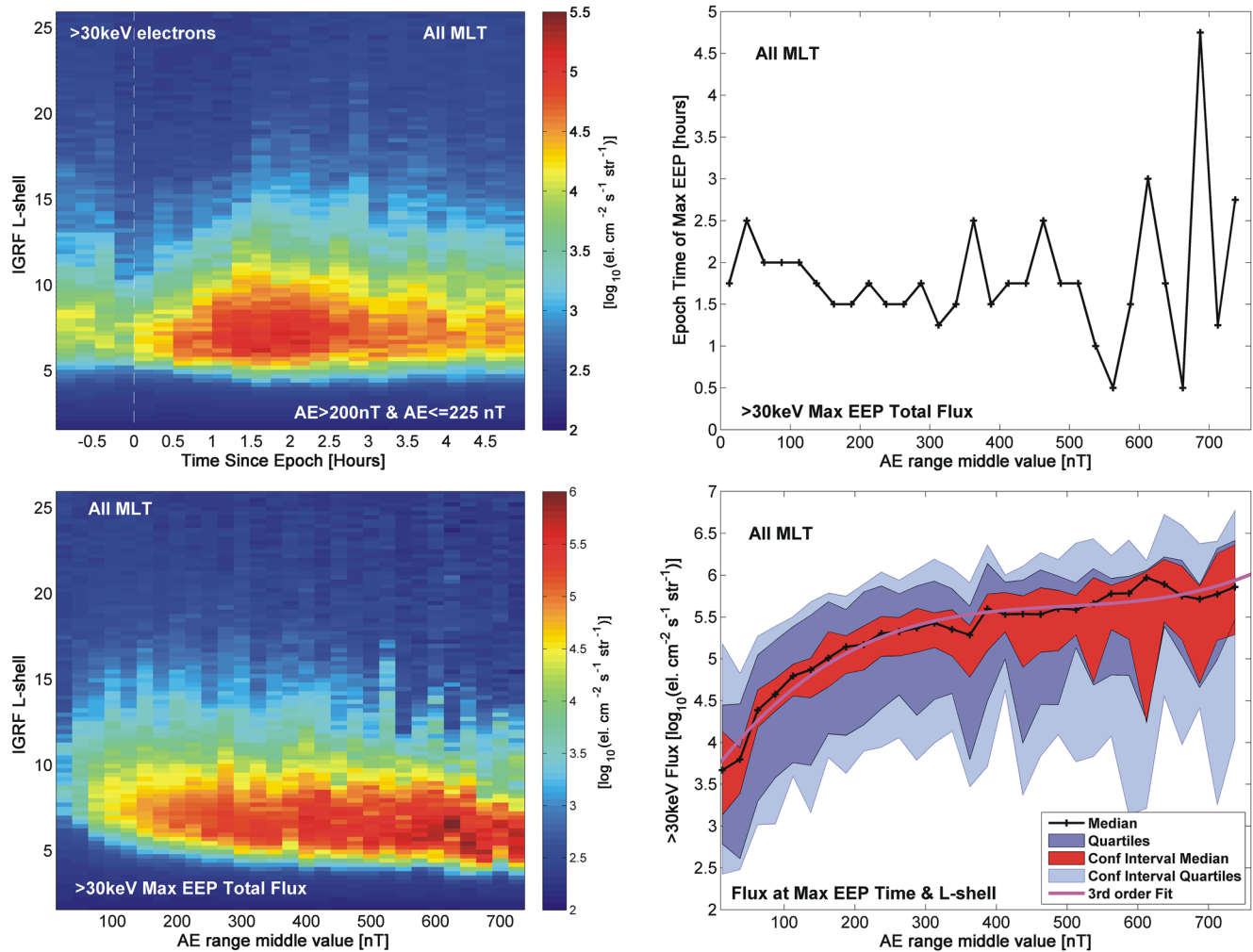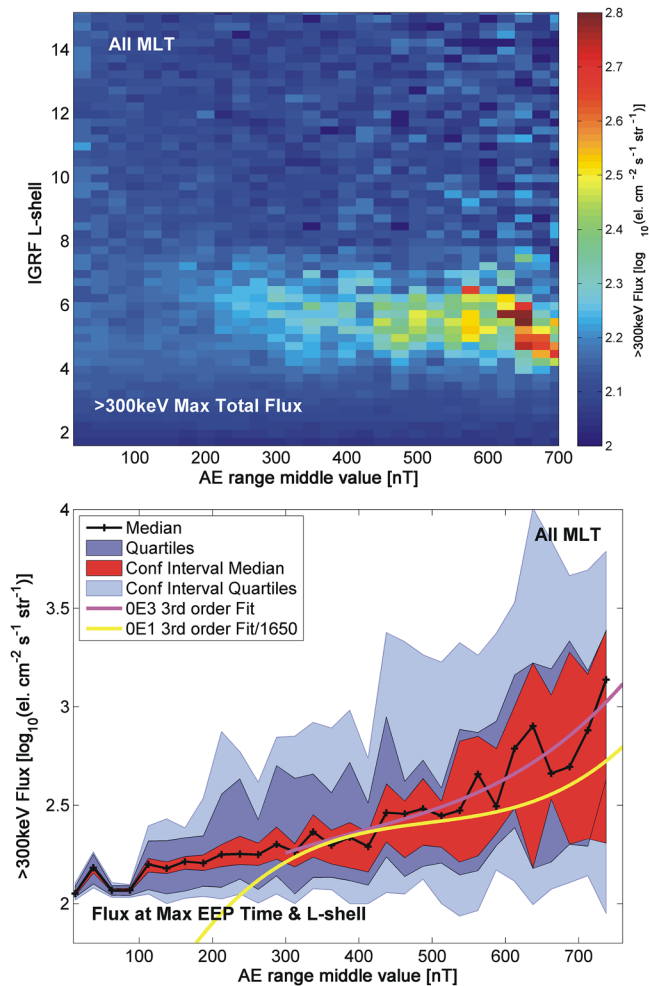
Figure 8. Examination of the variation in peak >30 keV fluxes EEP magnitude with respect to changing AE. Top left: SEA of the >30 keV EEP for the AE range from 200 to 225 nT. Bottom left: L- and AE-variation in 30 keV EEP fluxes at the times where the summed EEP fluxes are maximum for each AE-range. Top-right: Variation in epoch time when the summed EEP fluxes are maximum. Bottom-left: Statistical variability of the peak >30 keV EEP fluxes, using the same color scales as shown earlier (e.g., Figure 3). The magenta line is a 3-order polynomial fit to the median fluxes.

peak fluxes increase by two orders of magnitude, demonstrating the strong link between the EEP magnitudes in substorm clusters and the AE-value at the start of the cluster. The confidence interval around the median, shown in red in this panel, expands with increasing AE, likely reflecting the smaller number of events in the SEA with increasing AE. Flux magnitudes initially rise rapidly with increasing AE, and then more slowly, but without saturating (or reaching an asymptotic value) in the AE range considered. The magenta line in the panel is a 3-order polynomial fit to the line joining the median SEA flux magnitude results (black line), which closely matches its variation. The magenta line equation is given by:

$$\log_{10}(\text{EEP}) = 1.42 \times 10^{-8} \text{AE}^3 - 2.12 \times 10^{-5} \text{AE}^2 + 0.011 \, \text{AE} + 3.65 \tag{1}$$

where EEP is the >30 keV precipitating electron flux with units of $\text{cm}^{-2}\,\text{s}^{-1}\,\text{sr}^{-1}$, and AE is the AE index value with units of nT. As an example, for an AE value of 212.5 nT, Equation 1 suggests the peak EEP flux should be $1.47 \times 10^5 \, \text{cm}^{-2}\,\text{s}^{-1}\,\text{sr}^{-1}$, essentially the same as that observed ($1.5 \times 10^5 \, \text{cm}^{-2}\,\text{s}^{-1}\,\text{sr}^{-1}$, as noted above).

The upper right panel of Figure 8 investigates how the timing of the peak summed EEP changes during the SEA time period (−1 to +5 hr), with respect to AE. The variability seen in this panel is less distinct and clear than that seen for the L-shell of the peak (i.e., Figure S3 in Supporting Information S1). At the lowest AE values the peak summed EEP fluxes occurs at +2–2.5 hr after the zero epoch, but occurring earlier for higher AE levels.

Figure 9. Examination of the variation in peak >300 keV fluxes EEP magnitude with respect to sweeping AE. Top left: *L*- and AE-variation in 300 keV EEP fluxes at the times where the summed EEP fluxes are maximum for each AE-range. Bottom-left: Statistical variability of the peak >300 keV EEP fluxes, using the same color scales as shown earlier. The magenta line is a 3-order polynomial fit to the median fluxes, while the yellow line is the >30 keV fit shown in Figure 8 divided by 1,650.

For the AE range 300–325 nT (i.e., mid-point of 312.5 nT), the peak summed EEP fluxes occurs at +1.25 hr after the zero epoch, and thus roughly an hour earlier. This pattern does not continue for higher AE ranges, however, and the peak timing is found both earlier and later. This likely reflects higher statistical variation caused by smaller numbers of events in the SEA; for 600–625 nT there are only 41 clusters included in the SEA. On the basis of this panel we caution that is not clear that the peak flux timing moves earlier with increasing AE, indeed, it might be argued more simply from this figure that the peak precipitation typically occurs at +1.5–2 hr after the epoch.

5.2. >300 keV Electron Precipitation

We now undertake similar analysis as was considered above for the >30 keV EEP for the >300 keV EEP flux channel. The result of this is shown in Figure 9. The upper panel of Figure 9 is equivalent to the lower left-hand panel in Figure 8. Note that a much small flux range is plotted (less than one order of magnitude above the instrument noise floor), as the EEP enhancements are much smaller than seen for the lower energy integral fluxes. In the upper panel of Figure 9 we also limit ourselves to a smaller *L*-shell range, as the EEP flux changes are only observed in radiation belt *L*-shells, and do not extend to higher *L* in the higher energy case. For the lowest AE ranges no enhancements are visible with substorm linked AE-values needing to reach ~150 nT before the >300 keV fluxes are seen to rise above noise-floor levels. While the >300 keV flux levels linked to substorm clusters seen in Figure 8 are significantly lower than those seen for >30 keV fluxes in Figure 8, it is apparent that the >300 keV flux magnitudes increase with increasing AE. There is also evidence that the L-shell of the peak EEP fluxes moves inwards with increasing AE, as was seen for the >30 keV EEP case. The L-shell of the peak >300 keV EEP flux is plotted in the right-hand panel of Figure S3 in Supporting Information S1. One intriguing feature of the *L*-shells of the peak EEP fluxes seen in Figures 8 and 9, and contrasted in Figure S3 in Supporting Information S1, is that they appear to be located at essentially the same *L*-shells for the two energy ranges. They also move inwards in the same way with respect to energy. Despite the very large differences in magnitude, this contrast suggests the same wave processes are scattering electrons in both energy ranges.

The lower panel of Figure 9 presents the AE dependence and statistical variability of the peak >300 keV EEP flux magnitudes in the same format as the lower right-hand panel of Figure 8. As noted above, at the lowest AE-values

the peak EEP are around the noise floor, but increase by ~1 order of magnitude across the AE range considered. As in the equivalent panel in Figure 8, the magenta line presents a 3-order order polynomial fit of the median peak EEP fluxes, showing strong evidence of increasing flux magnitudes with increasing AE. We only fit fluxes for AE > 300 nT, to ensure we are not impacted by the noise floor. In this case the fitted equation is given by:

$$\log_{10}(\text{EEP}) = 8.20 \times 10^{-9}\,\text{AE}^3 - 9.80 \times 10^{-6}\,\text{AE}^2 + 4.91 \times 10^{-3}\,\text{AE} + 1.44 \tag{2}$$

where EEP is the >300 keV precipitating electron flux with units of $cm^{-2}\,s^{-1}\,sr^{-1}$, and AE is again the AE index value with units of nT. Superimposed on the panel is Equation 1, but with the flux magnitudes divided by 1,650, shown by the yellow line. The magenta and yellow lines appear fairly similar, suggesting that the EEP spectra does not change significantly with changing AE. It is also clear that the >300 keV flux magnitudes do increase with increasing AE for substorm clusters, in contrast to the findings of Nesse Tyssøy, Partamies, et al. (2021). These results suggest the EEP energy spectra is roughly consistent with AE.

6. Discussion

As shown in Figure 2, and subsequent analysis, the >30 keV EEP magnitudes peak in the 9–12 MLT ("late morning") sector. This is roughly consistent with earlier studies into the MLT variation of the equatorial intensity of whistler mode chorus (e.g., Meredith et al. (2012)), although in that case the peak appears to shift with increasing AE from 8 to 10 MLT to 6–8 MLT. However, more recent studies, incorporating observations from the Van Allen probes flagship radiation belt mission have shifted the chorus equatorial intensity peak into the late morning sector, at roughly 2–5 MLT (Meredith et al., 2020). It is not currently clear if the differences between our AE and MLT dependent >30 keV EEP magnitudes following substorms contradict the studies looking at the variability of equatorial intensity whistler mode chorus, or not. While a shift of 7 MLT (i.e., ~100° in longitude) certainly seems considerable, we note that this is not an "apples with apples" comparison; here we focus on a clearly defined set of physical events driving precipitation, that is, clusters of substorms, rather any time period with disturbed geomagnetic AE values. We suggest a dedicated study into the variation of the equatorial intensity of whistler mode chorus following substorms would be of value, especially given the large high-quality datasets currently available.

The results presented in the current study suggest a possible route to create an AE index proxy-driven model to represent EEP following magnetospheric substorm clusters. Such a model would be *L*- and MLT-dependent, able to capture the comparatively "fast" changes in EEP magnitudes occurring during recurrent substorms, as well as include an indication of the statistical variability in the EEP-input. While our focus has been on clusters of recurrent substorms rather than isolated events, it should be sufficient to capture the primary impact of substorm EEP; previous studies have shown that isolated substorms are roughly as common as substorm clusters (Rodger et al., 2016, Table 1), but produce ~1–2 orders of magnitude smaller EEP magnitudes in each event (Rodger et al., 2016, Figure A1).

Previous proxy-driven EEP representations have been coupled to global atmospheric chemistry climate models, with varying levels of success (see e.g., Nesse Tyssøy, Sinnhuber, et al. (2021)). Those EEP representations likely include substorm-driven EEP in an "averaged" or "smeared out" fashion, and more detailed work is required to determine if the averaging adequately captures the EEP-impacts. One example of this question is the large MLT-dependence expected in EEP, as all plasma wave drivers of precipitation have very strong MLT occurrence variations. van de Kamp et al. (2018) put forward a MLT-dependent medium energy EEP representation, suitable for coupling into long term atmospheric and climate modeling. Subsequent chemical modeling found that daily zonal-mean electron forcing provides a sufficiently accurate ozone response in long-term climate simulations, with only small differences in the ozone responses to the MLT-dependent and the MLT-independent forcings (Verronen et al., 2020). The same atmospheric study noted the importance of capturing the MLT variability in preparing the EEP input, noting "Even when atmospheric simulations can be made with a zonal-mean MEE forcing, it is important to apply a forcing that provides the correct total amount of energy input, and this requires flux measurements that have an adequate MLT coverage". We note also that this conclusion is specifically focused on long term ozone responses in climate simulations; a study focused on ionospheric rather than atmospheric impacts could well produce very different conclusions.

The SEA analysis undertaken here shows a decrease in the >30 keV EEP flux starting just before the zero epoch, for all AE ranges and MLT-sectors. We speculate that processes occurring before the substorm expansion phase, that is, during the substorm growth phase (Rostoker et al., 1980), could damp plasma wave activity, and hence generate the observed decrease in precipitation fluxes. Some justification for this speculation comes from the observation that the flux decreases are largest in the 9–12 MLT sector where chorus wave activity dominates. This pre-zero epoch precipitation decrease becomes weaker with increasing AE, which may mean the convection provided by solar pre-conditioning dominates the EEP driver during this time for higher AE conditions, overcoming the impact of the substorm growth phase. We note that that this suggestion is rather speculative. However, the pre-zero epoch flux decrease is a striking feature in the data, requires a definitive explanation, and could be the focus of future detailed consideration.

A recent study has modeled the SEM-2 MEPED telescopes, and concluded there may be significant problems with measurements by the 0-degree telescope which is commonly taken to provide bounce loss cone fluxes. To quote Selesnick et al. (2020): ".... the 0° telescope usually measures stably trapped or quasi-trapped (drift loss cone) electrons, rather than precipitating (bounce loss cone) electrons as would be expected based on its

orientation. (Exceptions occur when pitch angle diffusion is sufficiently enhanced, or when even the 90° telescope measures precipitating electrons.)". This might suggest that the 0eX data is essentially meaningless, and is simply providing information on the trapped/drift loss cone fluxes monitored by the 90eX telescope (which were previously analyzed around substorm clusters by Rodger et al. (2022)). At first glance the conclusions of Selesnick et al. (2020) appear extraordinary, given there have been roughly 20 years of studies employing the SEM-2 MEPED 0eX data as an indication of EEP (starting from Koontz et al. (2001)). Nonetheless, the conclusions deserve serious consideration and investigation due to the potential impact.

Based on the conclusions of Selesnick et al. (2020), one might expect that the variability in the 0eX data mirrors that in the 90eX data. Looking at the literature, one can find many examples where the 90eX and 0eX data are plotted alongside one another for the same time period or following the same analysis (examples are: Clilverd et al. (2010); Meredith et al. (2011); Hendry et al. (2012); Turner et al. (2012); Hardman et al. (2015); Neal et al. (2015); Søraas et al. (2018)). Looking at those plots, it is not uncommon for the 90eX and 0eX data to show strong similarities in time, that is, very similar time variability is seen in both datasets. That would, of course, be consistent with the idea that the 0eX data reported is dominated by contamination from the 90eX measurements. However, and as mentioned by Selesnick et al. (2020), this is also expected during intense scattering events (i.e., strong diffusion). During these time periods stably trapped electrons with relatively high pitch angles (mirroring close to the geomagnetic equator) will be scattered to much lower pitch angles and hence lower altitudes, passing through the 90eX telescopes pitch angle range on the way to the 0eX telescopes and precipitating into the atmosphere. In fact, precipitating particles must, almost by definition, be scattered from the trapped populations thus if the scattering process is considered to be stochastic (i.e., scatters a given proportion of the trapped population), then the variability in the precipitating fluxes will have a strong component of the variability of the trapped population. This has been observed in the case of EMIC-wave driven EEP, with sharp peaks in both telescopes (e.g., Carson et al., 2012; Hendry et al., 2017). Despite having all the hallmarks of Selesnickstyle potential contamination, the precipitation was subsequently confirmed by sharply defined events observed in ground based data (e.g., Clilverd et al., 2015; Hendry et al., 2016; Rodger et al., 2015). We also note that the papers presenting 90eX and 0eX data side by side show both similarities and differences, including times where the 90eX fluxes are high without corresponding increases in 0eX data.

Finally, we note there is existing impendent evidence that the 0eX fluxes are representative of EEP fluxes and not dominated by contamination. In the last 5–10 years there have been efforts to use the 0eX electron flux data to provide EEP as an energy input into the atmosphere (see the discussion in van de Kamp et al. (2018) and Nesse Tyssøy, Sinnhuber, et al. (2021)). That has involved a significant effort around the validation of the 0eX electron fluxes, often by comparing ground-based or atmospheric observations against the impact expected from the POES SEM-2 MEPED 0eX observations (examples being Clilverd et al. (2010), Neal et al. (2015), Rodger et al. (2013), and Clilverd et al. (2020)), effectively cross-calibrating the 0eX data against independent datasets. While those studies have identified issues with the POES 0eX observations, they have generally found that the POES SEM-2 reported EEP fluxes are meaningful, particularly at times of strong scattering - similar to the scattering produced by whistler mode chorus considered in our current study. Indeed, independent evidence from three different atmospheric or ionospheric measurements, that is, cosmic noise absorption, chemical species concentrations, and subionospheric radiowave propagation perturbations, do not support the idea that the POES 0-deg detector is reporting excessively large/false fluxes (Rodger et al. (2013), Nesse Tyssøy et al. (2016), and Clilverd et al. (2020)). One consistent conclusion of those studies is that the POES reported EEP is an underestimate of the "real" precipitation level into the atmosphere not a contamination-dominated over-estimate as suggested by the Selesnick et al. (2020) study.

We now turn to the SEA undertaken in the current study. For the quiet AE SEA results, there are some similarities and differences between the 90e1 and 0e1 SEA fluxes. This includes small increases in the 0e1 EEP flux starting at the zero epoch for the 21–24 MLT range at a time when the 90e1 EEP fluxes decrease. For the high flux, strong AE (AE ≥ 300 nT) disturbances, we acknowledge there are strong similarities in the time dependence of the 90e1 and 0e1 SEA fluxes. This could simply be due to the strong scattering situations occurring for these high AE cases. While we believe the previous literature described in detail above is strongly suggestive that the 0e1 fluxes are most likely to be "real" in this case, and not meaningless, we cannot currently rule out the possibility that there is significant contamination present, as suggested by Selesnick et al. (2020).

7. Summary

In this study we have examined the precipitation of energetic electrons around the times of substorm clusters. Using many decades of low Earth orbit satellite observations we have determined the typical behavior of EEP around these events, as well as the statistical variability, focused on the MLT, AE, and L-shell dependence. We undertook an analysis route informed by the knowledge that substorms trigger chorus waves which have strong MLT, AE, and L-shell dependence. We employed the same dataset of substorm clusters that have earlier been used to examine the variability in trapped radiation belt fluxes linked to recurrent substorm activity (in our earlier study, Rodger et al. (2022)). That earlier study concluded substorm clusters associated with quiet AE disturbances (AE ≤ 100 nT) produced no increases in energetic, relativistic, or ultra-relativistic electron trapped flux in the outer radiation belts. Whereas substorms which occur linked to moderate (100 nT < AE ≤ 300 nT) or strong AE (AE ≥ 300 nT) disturbances are clearly geoeffective in terms of radiation belt trapped flux enhancements. In contrast, this study finds that quiet, moderate, and strong AE disturbance substorm clusters all produce clear EEP enhancements immediately following the cluster onset.

The MLT-dependent analysis shows a well-defined MLT-dependent variation in >30 keV EEP magnitude, which is largely consistent across the AE-ranges considered. The EEP magnitude varies by several orders of magnitude depending on MLT, with a distinct and deep minimum in the late afternoon sector (15–18 MLT), and maxima in the mid to late morning sector (6–12 MLT). The MLT and L-occurrence of >30 keV EEP varies in a similar, if not identical way, to that seen earlier in the variation of lower band whistler mode chorus intensities. The strong similarity between the intensity of whistler mode chorus reported in the literature and >30 keV EEP magnitudes reported in the current study suggests the precipitation during these events is dominated at all MLT by plasma wave pitch angle scattering, rather than field line curvature scattering.

Clusters of substorms reliably produce enhancements in electron precipitation for >30 keV and >300 keV, with steadily increasing peak precipitation magnitudes with increasing AE. The peak precipitation flux L-shell also clearly moves inwards with increasing AE, in a highly similar way for the two energy ranges. The relationships between the peak >30 keV and >300 keV precipitating fluxes and AE are fairly similar, suggesting the precipitation spectra does not vary significantly with AE. This finding provides the basis required to specify the energy spectrum of EEP by plasma wave pitch angle scattering during substorm events.

We suggest the current study of the average magnitudes and statistical variability in the EEP parameters could be employed to further the examination of the relative importance of substorms to ozone variability in the mesosphere and upper stratosphere. Given those influences, it could also be used to provide a route for building an EEP model to represent precipitation driven by substorm clusters to be linked to atmospheric coupled chemistry and climate simulations.

Data Availability Statement

Data availability is described and accessible through the following websites: https://www.ngdc.noaa.gov/stp/satellite/poes/dataaccess.html (POES SEM observations), https://www.ukssdc.ac.uk/cgi-bin/wdcc1/secure/geophysical_parameters.pl (geomagnetic indices from the UK Solar System Date Centre).

References

Akasofu, S. I. (1981). Energy coupling between the solar wind and the magnetosphere. *Space Science Reviews*, *28*(2), 121–190. https://doi.org/10.1007/BF00218810

Andersson, M., Verronen, P. T., Rodger, C. J., Clilverd, M. A., & Seppälä, A. (2014). Missing driver in the Sun–Earth connection from energetic electron precipitation impacts mesospheric ozone. *Nature Communications*, *5*(1), 5197. https://doi.org/10.1038/ncomms6197

Andersson, M. E., Verronen, P. T., Wang, S., Rodger, C. J., Clilverd, M. A., & Carson, B. R. (2012). Precipitating radiation belt electrons and enhancements of mesospheric hydroxyl during 2004–2009. *Journal of Geophysical Research*, *117*(D9), D09304. https://doi.org/10.1029/2011JD017246

Aryan, H., Agapitov, O. V., Artemyev, A., Mourenas, D., Balikhin, M. A., Boynton, R., & Bortnik, J. (2020). Outer radiation belt electron lifetime model based on combined Van Allen Probes and cluster VLF measurements. *Journal of Geophysical Research: Space Physics*, *125*(8), e2020JA028018. https://doi.org/10.1029/2020JA028018

Asikainen, T., & Ruopsa, M. (2016). Solar wind drivers of energetic electron precipitation. *Journal of Geophysical Research: Space Physics*, *121*(3), 2209–2225. https://doi.org/10.1002/2015JA022215

Baker, D. N., Blake, J. B., Klebesadel, R. W., & Higbie, P. R. (1986). Highly relativistic electrons in the Earth's outer magnetosphere, I. Lifetimes and temporal history 1979–1984. *Journal of Geophysical Research*, *91*(A4), 4265–4276. https://doi.org/10.1029/JA091iA04p04265

Baumgaertner, A. J. G., Jöckel, P., Aylward, A. D., & Harris, M. J. (2013). Simulation of particle precipitation effects on the atmosphere with the MESSy model system. In F.-J. Lübken (Ed.), *Climate and weather of the Sun-Earth system (CAWSES)* (pp. 301–316). Springer Atmospheric Sciences. https://doi.org/10.1007/978-94-007-4348-9_17

Beharrell, M. J., Honary, F., Rodger, C. J., & Clilverd, M. A. (2015). Substorm-induced energetic electron precipitation: Morphology and prediction. *Journal of Geophysical Research: Space Physics*, *120*(4), 2993–3008. https://doi.org/10.1002/2014JA020632

Borovsky, J. E. (2016). In G. V. Khazanov (Ed.), *Solar wind-magnetosphere interaction, in Space weather fundamentals* (pp. 47–73). CRC Press. https://doi.org/10.1201/9781315368474-5

Carson, B. R., Rodger, C. J., & Clilverd, M. A. (2012). POES satellite observations of EMIC-wave driven relativistic electron precipitation during 1998–2010. *Journal of Geophysical Research*, *118*(1), 232–243. https://doi.org/10.1029/2012JA017998

Claudepierre, S. G., Ma, Q., Bortnik, J., O'Brien, T. P., Fennell, J. F., & Blake, J. B. (2020). Empirically estimated electron lifetimes in the Earth's radiation belts: Van Allen probe observations. *Geophysical Research Letters*, *47*(3), e2019GL086053. https://doi.org/10.1029/2019GL086053

Clilverd, M. A., Duthie, R., Hardman, R., Hendry, A. T., Rodger, C. J., Raita, T., et al. (2015). Electron precipitation from EMIC waves: A case study from 31 may 2013. *Journal of Geophysical Research: Space Physics*, *120*(5), 3618–3631. https://doi.org/10.1002/2015JA021090

Clilverd, M. A., Rodger, C. J., Gamble, R. J., Ulich, T., Raita, T., Seppälä, A., et al. (2010). Ground-based estimates of outer radiation belt energetic electron precipitation fluxes into the atmosphere. *Journal of Geophysical Research*, *115*(A12), A12304. https://doi.org/10.1029/2010JA015638

Clilverd, M. A., Rodger, C. J., Van de Kamp, M., & Verronen, P. T. (2020). Electron precipitation from the outer radiation belt during the St. Patrick's Day storm 2015: Observations, modeling, and validation. *Journal of Geophysical Research: Space Physics*, *125*(2), e2019JA027725. https://doi.org/10.1029/2019JA027725

Cresswell-Moorcock, K., Rodger, C. J., Kero, A., Collier, A. B., Clilverd, M. A., Häggström, I., & Pitkänen, T. (2013). A reexamination of latitudinal limits of substorm-produced energetic electron precipitation. *Journal of Geophysical Research: Space Physics*, *118*(10), 6694–6705. https://doi.org/10.1002/jgra.50598

Douma, E., Rodger, C. J., Blum, L. W., & Clilverd, M. A. (2017). Occurrence characteristics of relativistic electron microbursts from SAMPEX observations. *Journal of Geophysical Research: Space Physics*, *122*(8), 8096–8107. https://doi.org/10.1002/2017JA024067

Douma, E., Rodger, C. J., Blum, L. W., O'Brien, T. P., Clilverd, M. A., & Blake, J. B. (2019). Characteristics of relativistic microburst intensity from SAMPEX observations. *Journal of Geophysical Research: Space Physics*, *124*(7), 5627–5640. https://doi.org/10.1029/2019JA026757

Evans, D. S., & Greer, M. S. (2004). Polar orbiting environmental satellite space environment monitor - 2 instrument descriptions and archive data documentation, NOAA technical Memorandum version 1.4. *Space Environment Laboratory*.

Forsyth, C., Rae, I. J., Coxon, J. C., Freeman, M. P., Jackman, C. M., Gjerloev, J., & Fazakerley, A. N. (2015). A new technique for determining substorm onsets and phases from indices of the electrojet (SOPHIE). *Journal of Geophysical Research: Space Physics*, *120*, 10592–10606. https://doi.org/10.1002/2015JA021343

Forsyth, C., Rae, I. J., Murphy, K. R., Freeman, M. P., Huang, C.-L., Spence, H. E., et al. (2016). What effect do substorms have on the content of the radiation belts? *Journal of Geophysical Research: Space Physics*, *121*(7), 6292–6306. https://doi.org/10.1002/2016JA022620

Gjerloev, J. W. (2012). The SuperMAG data processing technique. *Journal of Geophysical Research*, *117*(A9), A09213. https://doi.org/10.1029/2012JA017683

Gjerloev, J. W., Hoffman, R. A., Friel, M. M., Frank, L. A., & Sigwarth, J. B. (2004). Substorm behavior of the auroral electrojet indices. *Annals of Geophysics*, *22*(6), 2135–2149. https://doi.org/10.5194/angeo-22-2135-2004

Gordon, E. M., Seppälä, A., & Tamminen, J. (2020). Evidence for energetic particle precipitation and quasi-biennial oscillation modulations of the Antarctic NO$_2$ springtime stratospheric column from OMI observations. *Atmospheric Chemistry and Physics*, *20*(11), 6259–6271. https://doi.org/10.5194/acp-20-6259-2020

Hardman, R., Clilverd, M. A., Rodger, C. J., Brundell, J. B., Duthie, R., Holzworth, R. H., et al. (2015). A case study of electron precipitation fluxes due to plasmaspheric hiss. *Journal of Geophysical Research: Space Physics*, *120*(8), 6736–6748. https://doi.org/10.1002/2015JA021429

Hendry, A. T., Rodger, C. J., & Clilverd, M. A. (2017). Evidence of sub-MeV EMIC-driven electron precipitation. *Geophysical Research Letters*, *44*(3), 1210–1218. https://doi.org/10.1002/2016GL071807

Hendry, A. T., Rodger, C. J., Clilverd, M. A., Engebretson, M. J., Mann, I. R., Lessard, M. R., et al. (2016). Confirmation of EMIC wave-driven relativistic electron precipitation. *Journal of Geophysical Research: Space Physics*, *121*(6), 5366–5383. https://doi.org/10.1002/2015JA022224

Hendry, A. T., Rodger, C. J., Clilverd, M. A., Thomson, N. R., Morley, S. K., & Raita, T. (2012). Rapid radiation belt losses occurring during high-speed solar wind stream–driven storms: Importance of energetic electron precipitation. In D. Summers, I. R. Mann, D. N. Baker, & M. Schulz (Eds.), *Dynamics of the Earth's radiation belts and inner magnetosphere* (pp. 213–224). https://doi.org/10.1029/2012GM001299

Jaynes, A. N., Baker, D. N., Singer, H. J., Rodriguez, J. V., Loto'aniu, T. M., Ali, A. F., et al. (2015). Source and seed populations for relativistic electrons: Their roles in radiation belt changes. *Journal of Geophysical Research: Space Physics*, *120*(9), 7240–7254. https://doi.org/10.1002/2015JA021234

Johnson, A. T., Shumko, M., Sample, J., Griffith, B., Klumpar, D., Spence, H., & Blake, J. B. (2021). The energy spectra of electron microbursts between 200 keV and 1 MeV. *Journal of Geophysical Research: Space Physics*, *126*(11), e2021JA029709. https://doi.org/10.1029/2021JA029709

Koontz, S. L., Bering, E. A., Evans, D. S., Katz, I., Gardner, B. M., Suggs, R. M., et al. (2001). Properties of the auroral zone ionosphere inferred using plasma contactor data from the international space station, 2001. *AGU Fall Meeting Abstracts*.

Li, W., Thorne, R. M., Angelopoulos, V., Bortnik, J., Cully, C. M., Ni, B., et al. (2009). Global distribution of whistler-mode chorus waves observed on the THEMIS spacecraft. *Geophysical Research Letters*, *36*(9), L09104. https://doi.org/10.1029/2009GL037595

Matthes, K., Funke, B., Andersson, M. E., Barnard, L., Beer, J., Charbonneau, P., et al. (2017). Solar forcing for CMIP6 (v3.2). *Geoscientific Model Development*, *10*(6), 2247–2302. https://doi.org/10.5194/gmd-10-2247-2017

Meredith, N. P., Cain, M., Horne, R. B., Thorne, R. M., Summers, D., & Anderson, R. R. (2003). Evidence for chorus-driven electron acceleration to relativistic energies from a survey of geomagnetically disturbed periods. *Journal of Geophysical Research*, *108*, 1248. https://doi.org/10.1029/2002JA009764

Meredith, N. P., Horne, R. B., Lam, M. M., Denton, M. H., Borovsky, J. E., & Green, J. C. (2011). Energetic electron precipitation during high-speed solar wind stream driven storms. *Journal of Geophysical Research*, *116*(A5), A05223. https://doi.org/10.1029/2010JA016293

Meredith, N. P., Horne, R. B., Shen, X.-C., Li, W., & Bortnik, J. (2020). Global model of whistler mode chorus in the near-equatorial region (|λm|< 18°). *Geophysical Research Letters*, *47*(11), e2020GL087311. https://doi.org/10.1029/2020GL087311

Meredith, N. P., Horne, R. B., Sicard-Piet, A., Boscher, D., Yearby, K. H., Li, W., & Thorne, R. M. (2012). Global model of lower band and upper band chorus from multiple satellite observations. *Journal of Geophysical Research*, *117*(A10), A10225. https://doi.org/10.1029/2012JA017978

Neal, J. J., Rodger, C. J., Clilverd, M. A., Thomson, N. R., Raita, T., & Ulich, T. (2015). Long-term determination of energetic electron precipitation into the atmosphere from AARDDVARK subionospheric VLF observations. *Journal of Geophysical Research: Space Physics*, *120*(3), 2194–2211. https://doi.org/10.1002/2014JA020689

Nesse Tyssøy, H., Sandanger, M. I., Ødegaard, L.-K. G., Stadsnes, J., Aasnes, A., & Zawedde, A. E. (2016). Energetic electron precipitation into the middle atmosphere—Constructing the loss cone fluxes from MEPED POES. *Journal of Geophysical Research: Space Physics*, *121*(6), 5693–5707. https://doi.org/10.1002/2016JA022752

Nesse Tyssøy, H., Sinnhuber, M., Asikainen, T., Bender, S., Clilverd, M. A., Funke, B., et al. (2021). HEPPA III intercomparison experiment on electron precipitation impacts: 1. Estimated ionization rates during a geomagnetic active period in April 2010. *Journal of Geophysical Research: Space Physics*, *126*, e2021JA029128. https://doi.org/10.1029/2021JA029128

Nesse Tyssøy, H. N., Partamies, N., Babu, E. M., Smith-Johnsen, C., & Salice, J. A. (2021). The predictive capabilities of the auroral electrojet index for medium energy electron precipitation. *Frontiers in Astronomy and Space Sciience*, *8*, 714146. https://doi.org/10.3389/fspas.2021.714146

Newell, P. T., & Gjerloev, J. W. (2011a). Evaluation of SuperMAG auroral electrojet indices as indicators of substorms and auroral power. *Journal of Geophysical Research*, *116*(A12), A12211. https://doi.org/10.1029/2011JA016779

Newell, P. T., & Gjerloev, J. W. (2011b). Substorm and magnetosphere characteristic scales inferred from the SuperMAG auroral electrojet indices. *Journal of Geophysical Research*, *116*(A12), A12232. https://doi.org/10.1029/2011JA016936

Partamies, N., Tesema, F., Bland, E., Heino, E., Nesse Tyssøy, H., & Kallelid, E. (2021). Electron precipitation characteristics during isolated, compound, and multi-night substorm events. *Annals of Geophysics*, *39*(1), 69–83. https://doi.org/10.5194/angeo-39-69-2021

Pettit, J. M., Randall, C. E., Peck, E. D., & Harvey, V. L. (2021). A new MEPED-based precipitating electron data set. *Journal of Geophysical Research: Space Physics*, *126*(12), e2021JA029667. https://doi.org/10.1029/2021JA029667

Reeves, G. D., Spence, H. E., Henderson, M. G., Morley, S. K., Friedel, R. H. W., Funsten, H. O., et al. (2013). Electron acceleration in the heart of the Van Allen radiation belts. *Science*, *341*(6149), 991–994. https://doi.org/10.1126/science.1237743

Ripoll, J.-F., Claudepierre, S. G., Ukhorskiy, A. Y., Colpitts, C., Li, X., Fennell, J., & Crabtree, C. (2020). Particle dynamics in the Earth's radiation belts: Review of current research and open questions. *Journal of Geophysical Research: Space Physics*, *125*(5), e2019JA026735. https://doi.org/10.1029/2019JA026735

Rodger, C. J., Carson, B. R., Cummer, S. A., Gamble, R. J., Clilverd, M. A., Green, J. C., et al. (2010). Contrasting the efficiency of radiation belt losses caused by ducted and nonducted whistler-mode waves from ground-based transmitters. *Journal of Geophysical Research*, *115*(A12), A12208. https://doi.org/10.1029/2010JA015880

Rodger, C. J., Clilverd, M. A., Green, J. C., & Lam, M. M. (2010). Use of POES SEM-2 observations to examine radiation belt dynamics and energetic electron precipitation into the atmosphere. *Journal of Geophysical Research*, *115*(A4), A04202. https://doi.org/10.1029/2008JA014023

Rodger, C. J., Clilverd, M. A., Kavanagh, A. J., Watt, C. E. J., Verronen, P. T., & Raita, T. (2012). Contrasting the responses of three different ground-based instruments to energetic electron precipitation. *Radio Science*, *47*(2), RS2021–n. https://doi.org/10.1029/2011RS004971

Rodger, C. J., Clilverd, M. A., & McCormick, R. J. (2003). Significance of lightning-generated whistlers to inner radiation belt electron lifetimes. *Journal of Geophysical Research*, *108*(A12), 1462. https://doi.org/10.1029/2003JA009906

Rodger, C. J., Clilverd, M. A., Nunn, D., Verronen, P. T., Bortnik, J., & Turunen, E. (2007). Storm-time short-lived bursts of relativistic electron precipitation detected by subionospheric radio wave propagation. *Journal of Geophysical Research*, *112*(A7), A07301. https://doi.org/10.1029/2007JA012347

Rodger, C. J., Clilverd, M. A., Seppälä, A., Thomson, N. R., Gamble, R. J., Parrot, M., et al. (2010). Radiation belt electron precipitation due to geomagnetic storms: Significance to middle atmosphere ozone chemistry. *Journal of Geophysical Research*, *115*(A11), A11320. https://doi.org/10.1029/2010JA015599

Rodger, C. J., Clilverd, M. A., Thomson, N. R., Gamble, R. J., Seppälä, A., Turunen, E., et al. (2007). Radiation belt electron precipitation into the atmosphere: Recovery from a geomagnetic storm. *Journal of Geophysical Research*, *112*(A11), A11307. https://doi.org/10.1029/2007JA012383

Rodger, C. J., Cresswell-Moorcock, K., & Clilverd, M. A. (2016). Nature's grand experiment: Linkage between magnetospheric convection and the radiation belts. *Journal of Geophysical Research: Space Physics*, *121*(1), 171–189. https://doi.org/10.1002/2015JA021537

Rodger, C. J., Hendry, A. T., Clilverd, M. A., Forsyth, C., & Morley, S. K. (2022). Examination of radiation belt dynamics during substorm clusters: Activity drivers and dependencies of trapped flux enhancements. *Journal of Geophysical Research: Space Physics*, *127*(1), e2021JA030003. https://doi.org/10.1029/2021JA030003

Rodger, C. J., Hendry, A. T., Clilverd, M. A., Kletzing, C. A., Brundell, J. B., & Reeves, G. D. (2015). High-resolution in situ observations of electron precipitation-causing EMIC waves. *Geophysical Research Letters*, *42*(22), 9633–9641. https://doi.org/10.1002/2015GL066581

Rodger, C. J., Kavanagh, A. J., Clilverd, M. A., & Marple, S. R. (2013). Comparison between POES energetic electron precipitation observations and riometer absorptions: Implications for determining true precipitation fluxes. *Journal of Geophysical Research: Space Physics*, *118*(12), 7810–7821. https://doi.org/10.1002/2013JA019439

Rodger, C. J., Turner, D. L., Clilverd, M. A., & Hendry, A. T. (2019). Magnetic local time-resolved examination of radiation belt dynamics during high-speed solar wind speed-triggered substorm clusters. *Geophysical Research Letters*, *46*(17–18), 10219–10229. https://doi.org/10.1029/2019GL083712

Rostoker, G., Akasofu, S.-I., Foster, J., Greenwald, R. A., Kamide, Y., Kawasaki, K., et al. (1980). Magnetospheric substorms - Definition and signatures. *Journal of Geophysical Research*, *85*(A4), 1663–1668. https://doi.org/10.1029/ja085ia04p01663

Selesnick, R. S., Tu, W., Yando, K. B., Millan, R. M., & Redmon, R. J. (2020). POES/MEPED angular response functions and the precipitating radiation belt electron flux. *Journal of Geophysical Research: Space Physics*, *125*(9), e2020JA028240. https://doi.org/10.1029/2020JA028240

Seppälä, A., & Clilverd, M. A. (2014). Energetic particle forcing of the Northern Hemisphere winter stratosphere: Comparison to solar irradiance forcing. *Frontiers in Physics*, *2*, 25. https://doi.org/10.3389/fphy.2014.00025

Seppälä, A., Clilverd, M. A., Beharrell, M. J., Rodger, C. J., Verronen, P. T., Andersson, M. E., & Newnham, D. A. (2015). Substorm-induced energetic electron precipitation: Impact on atmospheric chemistry. *Geophysical Research Letters*, *42*(19), 8172–8176. https://doi.org/10.1002/2015GL065523

Seppälä, A., Clilverd, M. A., & Rodger, C. J. (2007). NOx enhancements in the middle atmosphere during 2003–2004 polar winter: Relative significance of solar proton events and the aurora as a source. *Journal of Geophysical Research*, *112*(D23), D23303. https://doi.org/10.1029/2006JD008326

Seppälä, A., Randall, C. E., Clilverd, M. A., Rozanov, E., & Rodger, C. J. (2009). Geomagnetic activity and polar surface air temperature variability. *Journal of Geophysical Research*, *114*(A10), A10312. https://doi.org/10.1029/2008JA014029

Simms, L., Engebretson, M., Clilverd, M., Rodger, C., Lessard, M., Gjerloev, J., & Reeves, G. (2018). A distributed lag autoregressive model of geostationary relativistic electron fluxes: Comparing the influences of waves, seed and source electrons, and solar wind inputs. *Journal of Geophysical Research: Space Physics*, *123*(5), 3646–3671. https://doi.org/10.1029/2017JA025002

Søraas, F., Sandanger, M. I., & Smith-Johnsen, C. (2018). NOAA POES and MetOp particle observations during the 17 March 2013 storm. *Journal of Atmospheric and Solar-Terrestrial Physics*, *177*, 115–124. https://doi.org/10.1016/j.jastp.2017.09.004

Stepanov, N. A., Sergeev, V. A., Shukhtina, M. A., Ogawa, Y., Chu, X., & Rogov, D. D. (2021). Ionospheric electron density and conductance changes in the auroral zone during substorms. *Journal of Geophysical Research: Space Physics*, *126*(7), e2021JA029572. https://doi.org/10.1029/2021JA029572

Thorne, R., Ni, B., Tao, X., Horne, R. B., & Meredith, N. P. (2010). Scattering by chorus waves as the dominant cause of diffuse auroral precipitation. *Nature*, *467*(7318), 943–946. https://doi.org/10.1038/nature09467

Thorne, R. M., Li, W., Ni, B., Ma, Q., Bortnik, J., Chen, L., et al. (2013). Rapid local acceleration of relativistic radiation belt electrons by magnetospheric chorus. *Nature*, *504*(7480), 411–414. https://doi.org/10.1038/nature12889

Turner, D., Shprits, Y., Hartinger, M., & Angelopoulos, V. (2012). Explaining sudden losses of outer radiation belt electrons during geomagnetic storms. *Nature Physics*, *8*(3), 208–212. https://doi.org/10.1038/nphys2185

Van de Kamp, M., Rodger, C. J., Seppälä, A., Clilverd, M. A., & Verronen, P. T. (2018). An updated model providing long-term data sets of energetic electron precipitation, including zonal dependence. *Journal of Geophysical Research: Atmospheres*, *123*(17), 9891–9915. https://doi.org/10.1029/2017JD028253

Van de Kamp, M., Seppälä, A., Clilverd, M. A., Rodger, C. J., Verronen, P. T., & Whittaker, I. C. (2016). A model providing long-term data sets of energetic electron precipitation during geomagnetic storms. *Journal of Geophysical Research: Atmospheres*, *121*(20), 12520–12612. https://doi.org/10.1002/2015JD024212

Verronen, P. T., Marsh, D. R., Szeląg, M. E., & Kalakoski, N. (2020). Magnetic-local-time dependency of radiation belt electron precipitation: Impact on ozone in the polar middle atmosphere. *Annals of Geophysics*, *38*(4), 833–844. https://doi.org/10.5194/angeo-38-833-2020

Walton, S. D., Forsyth, C., Rae, I. J., Meredith, N. P., Sandhu, J. K., Walach, M.-T., & Murphy, K. R. (2022). Statistical comparison of electron loss and enhancement in the outer radiation belt during storms. *Journal of Geophysical Research: Space Physics*, *127*(5), e2021JA030069. https://doi.org/10.1029/2021JA030069

Walton, S. D., Forsyth, C., Rae, I. J., Watt, C. E. J., Thompson, R. L., Horne, R. B., et al. (2021). Cross-L* coherence of the outer radiation belt during storms and the role of the plasmapause. *Journal of Geophysical Research: Space Physics*, *126*(10), e2021JA029308. https://doi.org/10.1029/2021JA029308

Whittaker, I. C., Clilverd, M. A., & Rodger, C. J. (2014). Characteristics of precipitating energetic electron fluxes relative to the plasmapause during geomagnetic storms. *Journal of Geophysical Research: Space Physics*, *119*(11), 8784–8800. https://doi.org/10.1002/2014JA020446

Yando, K., Millan, R. M., Green, J. C., & Evans, D. S. (2011). A Monte Carlo simulation of the NOAA POES medium energy proton and electron detector instrument. *Journal of Geophysical Research*, *116*(A10), A10231. https://doi.org/10.1029/2011JA016671

Zhao, W., Liu, S., Zhang, S., Zhou, Q., Yang, C., He, Y., et al. (2019). Global occurrences of auroral kilometric radiation related to suprathermal electrons in radiation belts. *Geophysical Research Letters*, *46*(13), 7230–7236. https://doi.org/10.1029/2019GL083944